DRAFT VERSION FEBRUARY 1, 2008
Preprint typeset using LaTeX style emulateapj v. 20/04/00

arXiv:astro-ph/0010401v1 19 Oct 2000

THE RELATIVE STAR FORMATION HISTORIES OF SPIRAL BULGES AND ELLIPTICAL GALAXIES IN THE HUBBLE DEEP FIELDS

RICHARD S. ELLIS[1]
Department of Astronomy, California Institute of Technology, Pasadena, CA 91125. rse@astro.caltech.edu

ROBERTO G. ABRAHAM[1]
Department of Astronomy, University of Toronto, 60 St. George Street, Toronto, ON M5S3H8, Canada.
abraham@astro.utoronto.ca

AND

MARK E. DICKINSON
Space Telescope Science Institute, 3700 San Martin Drive, Baltimore,MD 21218. med@stsci.edu
Draft version February 1, 2008

ABSTRACT

Hierarchical galaxy formation models make specific predictions concerning the relative assembly rates and star formation histories of spiral bulges and field ellipticals. Independently of the cosmological model and initial power spectrum of fluctuations, at all epochs the stellar populations in spiral bulges should be older and redder than those in typical ellipticals selected at the same redshift. To test this simple prediction, we analyze the internal optical colors of a complete sample of $I_{814}<24$ mag early-type and spiral galaxies from the Northern and Southern Hubble Deep Fields (HDF). The subset of galaxies in the Northern HDF are also investigated in the near-infrared using NICMOS photometry. We compare the central (inner 5% radius) colors of those spirals with clearly visible bulges with the integrated colors of ellipticals in our sample. Comparisons are possible to a redshift $z \simeq 1$ at which point well-defined bulges become difficult to locate. The reliability of determining bulge colors using central apertures is tested by considering the homogeneity of the pixel-by-pixel colors for typical cases and through comparisons based on the simulated appearance at moderate redshift of the local sample of de Jong. We show via these tests and by selecting HDF subsets chosen according to inclination that disk contamination effects should be minimal. While spiral bulges are systematically redder in their optical colors than their associated disks at all redshifts, we find that the majority are significantly bluer than the red locus occupied by most field ellipticals at similar redshifts. In the near-infrared, similar trends are found at redshifts $z < 0.6$, but at higher redshifts some bulges as red as the reddest ellipticals are found. We conclude that a significant rejuvenation may have occurred in the inner stellar populations of many spiral galaxies, particularly those at intermediate redshifts. We examine the optical and near-infrared colors of the HDF bulges in the context of models which include the effects of secondary star formation superimposed upon pre-existing old populations and conclude the data is best fit when this secondary activity is burst-like. We discuss the consequences for models of secular evolution in disks should these bursts have been particularly prevalent at $z \simeq 0.6$ as the limited HDF data seems to imply.

1. INTRODUCTION

The origin of galactic bulges is an important and unsolved issue in our understanding of galaxy evolution. The hitherto established view is that galactic bulges form at high redshifts through early dissipationless collapse (Eggen, Lynden-Bell, & Sandage 1962, hereafter ELS). This is based principally on the evidence for old stellar populations concentrated in the bulge of our own Galaxy and contrasts with more recently-developed hierarchical galaxy formation models (Kauffmann et al 1993, Baugh et al 1998) where elliptical galaxies form from the merger of early disk systems which can, in turn, continue to accrete gas to form a two component spiral galaxy.

A robust prediction of all hierarchical models is that spiral bulges should, on average, contain older stars than their associated disks which form by subsequent accretion. Moreover, statistically at a given redshift, bulges should be older and redder than field ellipticals which predominantly form from the merger of previously created spirals. Importantly, these conclusions should remain valid regardless of the particular cosmological model or initial power spectrum which governs the rate of assembly of massive galaxies. As such, a comparison of the relative colors of ellipticals and spiral bulges offers a remarkably simple, but powerful, test of hierarchical assembly models.

A third alternative for the origin of stellar bulges proposes their manufacture via various instabilities of pre-existing disks (see the recent review by Combes 1999). Of greatest interest here is the suggestion that bulges may form through secular processes (those whose timescale are longer than the dynamical time), mostly through interactions and the evolution of galactic bars. Galactic bars can be transformed into bulges through a vertical heating of the inner disk via resonant scattering of stellar orbits by the bar potential. Numerical work also suggests that bulges may form via bar destruction through the growth and subsequent collapse of bar instabilities in cold rotating disks. Evidence that such secular activity may play an important role in the formation of bars is growing (Kormendy 1993; Kuijken & Merrifield 1995; Norman, Sellwood, & Hasan 1996) and there is rather good dynamical evidence that most bulges in very late-type galaxies are not true bulges, but rather vertically heated central disks (Kormendy 1993). This suggests that the relative importance of the three bulge formation processes may be a strong function of Hubble type.

[1]Also: Institute of Astronomy, University of Cambridge, Madingley Road, Cambridge, CB3 OHA, United Kingdom

Most investigators of bulge formation have sought to infer their origin by studying the stellar populations or dynamical properties of local galaxies. Of particular importance in this regard are extinction-free near-infrared imaging observations of the Milky Way bulge (Dwek et al 1995) and resolved studies of associated stellar populations (eg. Rich 1997). These studies and those possible for nearby galaxies have emphasized a much greater diversity in color and stellar history than had hitherto been believed (Wyse et al 1997) although the effects of dust and other factors remain unresolved (Peletier et al 1999).

Through the Hubble Deep Field (HDF) campaigns (Williams et al 1996, 1999), high resolution imaging data is now available with sufficient signal-to-noise to enable the direct study of bulge growth and evolution *in situ* to redshifts $z \sim 1$. Given the above discussion, it is clear that a detailed observational comparison of the resolved stellar populations of field spirals and ellipticals as a function of redshift will offer important insight into some of the most fundamental aspects of galaxy formation. Indeed, only via intermediate redshift data can the epoch corresponding to the formation of the bulge component be determined independently of the age of its stars.

In an earlier paper (Abraham et al. 1999a) we investigated the importance of secular processes in forming bulges by determining the proportion of barred spiral galaxies in the Hubble Deep Fields as a function of redshift, finding a tentative decline in the fraction of barred galaxies beyond redshift $z \simeq 0.5$. The physical mechanisms responsible for such a deficit of barred spirals at high redshift remain unclear. Possibilities include dynamically hotter (or increasingly dark-matter dominated) disks or an enhanced efficiency in bar destruction at high redshift. Regardless, the absence of bars at high redshift does seem to pose an observational challenge for models where bulges form via secular activity initiated by bars. Such activities may be episodic (Sellwood 1999), or confined to low-luminosity late-type spirals (Kormendy 1993) which are too faint at high redshifts to have been included in our earlier investigation.

In a precursor of this study (Abraham et al. 1999b), the dispersion in the internal colors of a sample of high-redshift HDF spirals with redshifts was used to investigate the relative colors and star-formation histories of bulges and disks at high redshifts. This work concluded that bulges are redder and older than their surrounding disks in essentially all luminous high-redshift spirals. However, while bulges appear redder than their surrounding disks out to high redshifts, no investigation of the relative colors of bulges and ellipticals as a function of redshift was undertaken at that time.

Such a comparison forms the basis of this paper. Here we continue our HDF investigations concerning the origin of galactic bulges by measuring the relative colors of spiral bulges and ellipticals as a function of photometric and spectroscopic redshift. Using automated morphological classifications, our study includes a total sample of 95 spirals and 60 early-type galaxies with $I_{814} < 24$ mag in the Northern and Southern Hubble Deep Fields. An additional aspect of this work is the augmentation of our optical data by near-infrared NICMOS observations (Dickinson 2000) of a subset of our data, extending coverage into the J_{F110W} and H_{F160W} photometric bands in the Northern Hubble Deep Field. These infrared observations are neither as deep nor as well-sampled as the optical data in the HDF-N, but provide a number of interesting constraints on the conclusions derived from optical photometry alone.

A plan of this paper follows. In §2 we describe our overall sample selection and the techniques used to assign redshifts to these galaxies. In §3 we describe our technique for estimating the relative colors of ellipticals and bulges via the measurement of a central aperture $V_{606} - I_{814}$ color. We quantify the uncertainty in these estimates for the bulges in our sample by examining individual cases and applying a similar technique to the local spiral galaxy sample of de Jong (1996). We discuss the bulge-elliptical comparison in the context of hierarchical models in §4 and summarize our main conclusions in §5.

2. THE HDF SAMPLE

As in Abraham et al (1999a,b), we take advantage of the unique nature of both Hubble Deep Fields (HDFs, Williams et al 1996, 1999). The long exposures in these observations guarantees substantially improved signal to noise in several passbands over earlier multi-color HST imaging surveys such as the Medium Deep Survey (Ratnatunga et al 1999). This is particularly important in the reliable separation of ellipticals from spiral bulges with low surface brightness disks. The 0.04 arcsec/pixel sampling of the drizzled optical data makes isolation of the bulge comparatively easy, as described below (§3). By combining both HDFs, a larger sample is produced which is essential for statistical comparisons such as the color evolution of bulges and ellipticals at a given redshift.

For the Northern HDF field, we supplement our optical data with near-infrared NICMOS data. (The characteristics of these data are described in Dickinson 2000, and are only summarized here.) Although the HDF-N was observed in the near-infrared from the ground in several programs, the depth and angular resolution of these data ($\simeq$1 arcsec FWHM) are a poor match to that of the optical WFPC2 images. The present NICMOS HST data was obtained by mosaicing the complete HDF-N with a mean exposure of 12600s per filter in F110W (1.1μm) and F160W (1.6μm). The sensitivity varies over the field of view but the mean depth is $AB \simeq 26.1$ at 10σ within a 0.7 arcsec diameter aperture. The drizzled NIC3 PSF has a FWHM = 0.22 arcsec and is primarily limited by the NIC3 pixel scale.

The I_{814} =24 mag limit adopted for the present morphological study is a conservative one. For example, Ratnatunga et al (1999) claim reliable morphological classifications are possible to I_{814} =26 mag in the northern HDF. An important consideration here is the reliable isolation of the bulge component at high redshifts. We defer discussion of this point to §3. However, we note at this point that bulges becomes difficult to reliably detect beyond a redshift $z \simeq 1$. As a significant fraction of galaxies beyond $I_{814} > 24$ have redshifts beyond unity, this is an additional justification for our adopted magnitude limit.

The baseline photometric catalogs for the present study are the publicly available `SExtractor` optical catalogs produced by the Space Telescope Science Institute (STScI). Throughout the present paper, we will adopt IAU-format object designations and coordinates keyed to these catalogs. To I_{814} = 24 mag, both HDF images contain 242 galaxies of all types. Morphological classification of this sample was undertaken using the automated classification technique (based on measures of central concentration and rotational asymmetry) described in Abraham et al. (1996a,b), supplemented by visual classifications determined by two of the authors (RSE and RGA). This is the same strategy adopted in our analysis of bar structure in the HDF fields (Abraham et al 1999a). The galaxies in our sample are sufficiently bright that there is no ambiguity in matching galaxies to their counterparts in the corresponding NICMOS image of the northern HDF.

Table 1 summarizes the properties of the full sample. The table records integrated and central optical and near-IR colors as defined later in the paper, quantitative structural measures (central concentration, rotational asymmetry, axial ratio, and automated classification), and visual classifications according to two of the authors (RSE and RGA). Visual classifications are on the MDS numerical system: -2=star, -1=compact, 0=E, 1=E/S0, 2=S0, 3=Sab, 4=S, 5=Scdm, 6=Ir, 7=peculiar, 8=merger, 9=defect. A measure of the uncertainties for the purpose in hand (selecting spirals and ellipticals) can be gained from comparisons of both visual classification schemes with that determined automatically.

Automated classification results in a sample of 95 spirals and 60 early-type systems, the remainder being irregulars, mergers or peculiars. Visual classification by RSE (RGA) results in a total of 96 (123) spirals and 74 (64) early-types. In the present paper visually classified intermediate type systems, ie. S0/a galaxies, were categorized as early-type. (Nine galaxies in total were classed as S0/a systems, and we will demonstrate in §4 that our results do not depend sensitively on how they are partitioned).

The RSE classes are in excellent agreement with those determined automatically for spirals but a 23% excess of ellipticals is found. Conversely, RGA finds good agreement with the automated scheme for ellipticals but has a 29% excess of spirals. This level of discrepancy is consistent with earlier comparisons between independent visual classifications of faint galaxies (Abraham et al. 1996b). Concerning the apparent discrepancies for spirals, it should be noted that the automated classifier is tuned to categorize weakly distorted systems and very late-type spirals as peculiar. The excess of visually-classified ellipticals is thought to arise because some visual classifiers weight global symmetry more than central concentration (Marleau & Simard 1999).

The most important consideration here is the selection of reliable samples of ellipticals and well-defined spirals (the latter from which the bulge properties can be determined). In the case of the ellipticals, we follow precisely the selection criteria of Abraham et al (1996,1999a) for the HDF-N and its equivalent procedure for the HDF-S (Menanteau et al 2000). Discussion of possible contamination of these elliptical samples by compact galaxies can be found in Menanteau et al (2000). In the present paper no attempt is made to separate S0s from ellipticals.

As described below, we will restrict our spiral sample to those non-peculiar systems with prominent bulges. For this subset both visual and automated classifications give virtually identical results so far as locating spirals is concerned. Regular spirals and those with visible bulges were ascertained by visual inspection by both observers. However, one of us (RGA) examined those spirals he classed in more detail for blending effects and these more detailed visual morphological classifications (summarized in Table 1) form the basis of the remainder of the analysis. The principal goal here is to enable selection of various (presumed "clean") subsets of spiral bulges for later analysis. We will show in §4 that the conclusions of this paper do not depend sensitively on the exclusive use of any one of these subsets.

For the RGA-classed spirals, the column denoted "`bulge?`" indicates the presence of a bulge component. The column denoted "`blend?`" indicates whether nearby companions or optical superpositions overlap with a galaxy image at a 2σ isophotal threshold on the I_{814} -band image. Blends are categorized as either "severe" or "minor". Severe blends are cases where the overlapping images cannot be reliably disentangled. The distinction between a "severe" blend and a merger is obviously rather subjective. In some cases tidal tails make the latter classification obvious, while conversely "severe blending" is appropriate when contamination originates from, *e.g.* a diffraction spike presenting photometric difficulties. The "minor" blend category encompasses systems where the overlapping images can be cleanly separated by raising the 2σ isophotal threshold, used to define the galaxy above the sky background, by a small amount (typically an additional 1–3σ above the sky noise level). The tabulated photometric parameters for galaxies flagged as minor blends in Table 1 correspond to the properties determined at this higher threshold. Throughout the remainder of this paper these minor blends will be treated in the same manner as isolated galaxies. The flag, "`pec?`" indicates the visual presence of an optical peculiarity that is insufficient to warrant classifying the galaxy as a peculiar, *eg.* a spiral that could reasonably be classed as Spec in local catalogs.

Figure 1 (Plate 1) presents a montage, ordered by I_{814} magnitude, of the 68 isolated non-peculiar systems classified as spirals by RGA whose bulge components are clearly visible, ie. systems selected from Table 1 using the following criteria: `(RGA = Sab, Sbc, or Disk)`, `bulge? = yes`, `pec? = no`, and `blend?` $\neq$ `severe`. We note that the prominent bulges and fairly tight spiral structure visible on many of the spirals shown Figure 1 indicates that the majority of systems are earlier than type Scd. This is of course consistent with our initial pre-selection designed to isolate spirals with prominent bulges.

Galaxy redshifts are listed on each panel of the montage. Spectroscopic redshifts become progressively fewer fainter than I_{814} =22.5 mag in the HDF-N and are still rather scarce in the HDF-S. We have therefore augmented the spectroscopic redshift estimates with photometric redshifts based on the publicly available catalog produced by Gwyn (`http://astrowww.phys.uvic.ca/grads/gwyn/pz/index.html`). These photometric redshifts are based on optical photometry only and do not include broad-band infrared colors. However, the summary of results in Hogg et al. (1999) suggests that infrared photometry does not significantly improve the accuracy of the photometric redshifts in the HDF for the $z < 1$ range of importance in this work.

3. PHOTOMETRIC DECOMPOSITION

Many studies of high-redshift bulges have attempted to decompose galaxian light into components by fitting analytical models to the surface brightness distributions of galaxy images (Schade et al 1995, Lilly et al 1998, Marleau & Simard 1998, Ratnatunga et al 1999). In this procedure, all pixels in the image are used to determine simultaneously the global structural parameters for all components of the galaxy, such as the scale lengths, ellipticities, and characteristic surface brightnesses for the bulge and disk. By integrating over the results from such fits, the colors of galactic components can be inferred.

Obtaining robust model fits using this technique can be challenging and, at a more fundamental level, the approach assumes the validity of canonical fitting laws and a close correspondence between stellar populations and global galactic structure (a relationship that is likely to vary reasonably strongly with Hubble type). Both of these may be poor assumptions, particularly for later Hubble types (Kormendy 1993). By utilizing all pixels in the image to determine model parameters this technique clearly

optimizes signal-to-noise, but of course this advantage can also prove a liability, as a small number of pixels affected by features not incorporated into the models (such as dust) can have a global impact on the fits. Furthermore, the morphological irregularity of high redshift galaxies suggests that fitting smooth light distributions to distant galaxies may introduce spurious results if care is not taken to first isolate underlying smooth features from superposed asymmetrical structures. This idea is very difficult to implement in a scale-free manner, although some attempts based on enforcing rotational symmetry seem quite encouraging (Schade et al. 1995; Lilly et al. 1998), and alternative fitting methods which attempt to minimize the effects of irregular features by adopting particularly robust minimization strategies (eg. simulated annealing) also show promise (Marleau & Simard 1998).

In the present paper, we choose to adopt a simpler approach which foregoes any attempt to determine the global structural parameters of the galaxies in our sample, in order to focus specifically on bulge stellar populations in a robust non-parametric manner. We estimate bulge colors by measuring the colors of the innermost regions of galaxy images where the bulge component dominates. This approach is conceptually similar to that adopted by Peletier et al. (1999) in determining bulge colors for local spirals using HST NICMOS observations, although the details (described below) differ.

Ideally an aperture selected to locate the bulge should be defined so as to be linked physically to the intrinsic properties of the galaxy. In this way correlations with, e.g. redshift, disk surface brightness and luminosity would be minimized. However, such an approach suffers from many of the difficulties associated with a full decomposition (see above) and, in practice, when observing with an instrument (WFPC-2) with a fixed pixel size, turns out to be very difficult to arrange. A metric aperture cannot easily be chosen to simultaneously avoid disk contamination at low z whilst containing an adequate number of HST pixels (from signal/noise considerations) at large redshift.

Instead we adopted an aperture size which scales with the isophotal size of the galaxy. This has the merit of great simplicity, the argument being that any systematic effects can be explored through careful simulations based on nearby galaxies. A potential drawback of this approach is that the nuclear colors so defined may be contaminated by disk light in a manner that is a function of redshift (assuming disks are generally bluer than bulges at high redshifts, cf. Abraham et al. 1999b). We show below from detailed simulations that, for the nuclear regions of low-inclination spirals with morphological T-types $T < 6$ (ie. Sc and earlier), bulge light dominates over disk light out to quite high redshifts in both V_{606} and I_{814} filters, so that the *central* $V_{606}-I_{814}$ color traces bulge colors with an RMS accuracy of $\sigma_{V-I} < 0.15$ mag out to $z < 0.7$.

Further tests we introduce to examine possible systematic effects are the analysis of subsets of our sample of spirals with prominent bulges defined in the previous section, restricted according to disk inclination and comparisons between optical and optical-infrared colors since disk contamination should be minimal in the latter case.

3.1. *Methodology*

In this section we describe the procedure used to analyze our primary WF/PC2 optical dataset. The analysis of our supplementary NICMOS observations of the HDF-N field proceeded along essentially identical lines. However, it is important to make clear at this stage that the under-sampling of the NIC3 detector relative to WF/PC2 observations, and the rather uncertain photometric calibration of the NICMOS instrument, make it substantially harder to apply the techniques described in this section to the NICMOS observations. For these reasons (and because the NIC3 data are restricted to HDF-N), in the present paper we will treat the NICMOS data as an interesting adjunct to our optical data that is mostly useful for testing and elaborating the conclusions derived at from data obtained at optical wavelengths, and defer further discussion of the NICMOS data until §5.4.

Our analysis is based on elliptical apertures defined using second order moments obtained from the I_{814}-band image of each galaxy in Table 1. These were used to define an ellipse whose area corresponds to that of the galaxy above a 2σ isophotal threshold. Large aperture ('total') colors (see Table 1) were defined using this procedure applied to the I_{814} image. For each galaxy a circular aperture was then defined with a radius of 5% of the semi-major axis length of the galaxy's ellipse, and this inner aperture was then used to determine the $V_{606}-I_{814}$ colors of the central portion of the galaxy.

The 5% isophotal radius aperture size was chosen according to the following considerations. Clearly the aperture should be as small as possible in order to isolate bulge light with a minimum of contamination from disk light. However the aperture must be large enough to encompass several pixels from signal/noise considerations. For a minimum of 10 pixels to be averaged, the aperture radius must be at least 2 pixels corresponding to an angular size of $\simeq 0.08''$ using the dithered $0.04''$ pixels of the Version 2 HDF images released by STScI. Assuming H_0=70 km sec^{-1} Mpc, Ω_M=0.3 and Ω_Λ=0.7 (the cosmology adopted throughout the paper), $0.08''$ corresponds to 0.64 kpc at z=1.

The location of each aperture was automatically adjusted by the measurement algorithm so as to be positioned on the local centroid of the galaxy image. The central and total $V_{606}-I_{814}$ colors for all galaxies in our sample (including ellipticals) are given in Table 1. The photometric zero points are given in Williams et al. (1996).

Initially we considered defining the bulge interactively for each galaxy by "growing" the bulge region out from the nucleus on a pixel-by-pixel basis, isolating the inner pixels of the galaxy whose resolved pixel-by-pixel color distribution was homogeneous at some pre-determined level. This methodology was found to work well for bright galaxies. However, as was found in Abraham et al. (1999b), the limiting magnitude for this approach in the HDF data is around I_{814} =23.2 mag, motivating us to attempt to improve the signal-to-noise of the measurement by binning together central pixels using central apertures in order to reach a practical magnitude limit of I_{814} =24 mag. Thus in the present paper the pure pixel-by-pixel approach is set aside in favor of a central aperture. It is important, nonetheless, to understand whether a 5% aperture radius allows us to chromatically isolate a typical bulge.

We can test this by examining the pixel-by-pixel optical colors in a number of bright galaxies as an independent check. Figure 2 shows how the bulge pixel colors are distributed with respect to those of the outer disk in 3 bright spirals with fractional aperture radii corresponding to 2%, 5% and 7% of the semi-major axis length. As can be seen, in all cases the bulge defined by a 5% radius is remarkably homogeneous and red compared to the pixels outside. In fact the relative colors of the

spiral bulge and the elliptical in the third and fourth rows (seen at virtually identical spectroscopically-determined redshifts of $z = 1.013$ and $z = 1.016$) foreshadows our major result: the bulge in the spiral system is significantly bluer than the typical elliptical.

3.2. *Possible Contamination of Bulge Colors by Disk Light*

The suitability of deriving bulge colors using a constant fractional aperture can be further assessed by considering the spirals in the local sample of de Jong (1996; hereafter DJ96). In this section we utilize analytic profile fits to the DJ96 sample photometry and estimate, on their basis, the likely disk contamination expected when the DJ96 galaxies are artificially placed at various redshifts and analysed with our central aperture technique.

DJ96 presents fundamental disk and bulge parameters in *BVRIHK* bands for 86 nearby low—intermediate inclination spiral galaxies as a function of Hubble T-type. The suitability of any currently-available local reference sample for the purposes of comparing with deep HST data is debatable, but the resolution and rest-frame depth of the data presented in DJ96 corresponds reasonably closely to that for deep images obtained with HST at high redshifts. The reader is referred to Lilly et al. 1998 (who also adopt DJ96 as the local calibration sample for a study of high redshift spirals) for a further discussion of this point.

It is also questionable whether an $r^{1/4}$-law profile or an exponential profile provides the most suitable description of local bulges. Following Frankston & Schild (1976) and Andredakis & Sanders (1994), DJ96 convincingly argue that local bulges are best fit by $r^{1/4}$ profiles in early-type spirals, and by exponential profiles in late-type systems, and presents fits based on both canonical profiles as a comparison. In order to undertake a more rigorous test of our methodology, and in order to estimate our measurement errors conservatively, in the present paper we will adopt the exponential-law profile fits given in DJ96. The sharp nuclear spike of the $r^{1/4}$ profile makes determining bulge colors on the basis of the technique described in the present paper more accurate.

Figure 3 illustrates the difference between the $U-V$ and $B-R$ bulge colors determined by 5%-isophotal radius aperture photometry and those determined by integrating over the DJ96 model fits. As de Jong (1996) does not tabulate model fits in U-band, we have assumed a constant rest-frame $U-B = -0.12$ mag for the disk component, and constant rest-frame $U-B = 0.50$ mag for the bulge component, corresponding to the mean colors for late and early-type galaxies in Table 1 of van den Bergh 1998. Note that U and B bands correspond roughly to rest-frame V_{606} at redshifts of $z \sim 0.4$ and $z \sim 0.7$, respectively, so the left and right panels of the figure illustrate the expected errors introduced into our $V_{606}-I_{814}$ bulge color measurements at these redshifts. On the basis of this figure, at $z \sim 0.4$ we can expect the RMS uncertainties on our bulge color estimates to be $\sigma_{V-I} < 0.1$ for spirals earlier than Sc, and $\sigma_{V-I} < 0.15$ for essentially all spirals earlier than type Sdm. At higher redshifts, blue rest-frame disk light may contaminate the bulge light to a larger degree, but even at $z \sim 0.7$ the RMS contamination is only $\sigma_{V-I} \sim 0.2$ for spirals earlier than Sc, which we will show below is substantially smaller than the typical color difference between ellipticals and bulges at the redshifts of interest. Using NICMOS $J_{110}-H_{160}$ colors, disk contamination is expected to be negligible at $z < 1$.

3.3. *Aperture Effects for the Elliptical Galaxies*

In order to facilitate the simplest comparison between the colors of spiral bulges and ellipticals, we will utilize integrated (i.e. large aperture) colors for the field ellipticals. As described earlier, large aperture colors were derived within ellipses defined by the second order moment of each galaxy in the I_{814} band. For completeness, Table 1 also lists 5% aperture photometry for these sources as this contains important information on the extent to which ellipticals represent a homogeneous population.

Abraham et al (1999b) found that as many as a third of the HDF ellipticals to $I_{814} = 23.2$ have cores bluer than those of the galaxies' periphery suggesting bursts of star formation involving at least a few percent of the galactic mass in the previous few Gyr. Because of this, the use of 5% aperture colors for the ellipticals would complicate any comparison with our sample of spiral bulges.

A complete discussion of the internal optical colors of the HDF elliptical population is presented in a separate paper (Menanteau et al 2000). Nonetheless it is interesting to examine the color inhomogeneities from Table 1 briefly in order to set a scale for the color variations we later discuss for spiral bulges. For the HDF ellipticals in the present study, the mean offset in color in the sense (aperture)-(total) is $\simeq$0.08 mag with $\simeq$15% showing no difference at all. Only 10% of the sample has offsets greater than 0.2 mag.

4. RELATIVE OPTICAL COLORS OF BULGES AND ELLIPTICALS

In this section we will investigate the optical colours of our complete sample of bulges and ellipticals, and defer consideration of the infrared subset of these data until §5.3.

The $V_{606}-I_{814}$ colors of ellipticals and spiral bulges as a function of photometric redshift are compared in Figure 4. This figure also shows the predicted colors of a simple passively-evolving stellar population based on the spectral synthesis models of Charlot & Bruzual (1999). This baseline model prediction corresponds to a single 1 Gyr burst at high redshift (z_F=3) and assumes solar metallicity with a Scalo Initial Mass Function. In Figure 4 the symbol sizes are keyed to central concentration and it is seen that most spirals in the sample are indeed prominently nucleated early-types, as expected from our initial pre-selection of spirals with prominent bulges.

The prominent red locus defined by some (but not all) of the ellipticals in Figure 4 shows a redshift-dependent trend consistent with earlier work (Schade et al 1996, 1999, Brinchmann et al 1998) and, with some exceptions, is in excellent agreement with our simple passively-evolving model. As discussed by Abraham et al (1999b), a significant fraction of ellipticals lie blueward of the well-defined red-locus. Many of these early-type systems have bluer nuclei and are thought to be remants of recent merging providing good evidence for continued formation of spheroid galaxies through mergers of late-type galaxies (Menanteau et al 2000, Brinchmann & Ellis 2000).

Contrary to expectations, the bulges in our sample of regular, isolated spirals show a systematic blueward scatter relative to the red early-type locus. Whereas both bulges and ellipticals show a dispersion in color at a given redshift, the distributions are characteristically different. A much smaller fraction of the elliptical population is blue although there is strong hint of a bimodality in the distribution, consistent perhaps with bursts or star formation associated with recent merging (Menanteau et al 2000). By contrast, few of the bulges occupy the 'red envelope'

region of the color - redshift relation as expected if they are intrinsically older than their elliptical counterparts. Moreover their distribution of colors is less bimodal and occupies the intermediate region, consistent on the one hand perhaps with less extreme evolutionary trends but on the other hand ones that are spread throughout the population.

Before accepting the surprising result that bulges are, as a population, systematically bluer than ellipticals in the mean, it is important to investigate possible sources of systematic error. The main source of systematic error is likely to be contamination from underlying disk light. As described in §3.2, the offset between typical bulge colors and the colors of red ellipticals is most significant for $z \lesssim 0.5$. At higher redshifts the bulk of the effect is unlikely to be explained fully by disk contamination unless the DJ96 is very unrepresentative of the high redshift spiral population. Other systematic effects can be best studied by introducing a measure of the color scatter of the bulges with respect to our baseline passively evolving high-redshift collapse model. We define a simple parameter characterizing the offset between a galaxy's observed color and the predicted color of our baseline high-redshift burst model:

$$\delta(V_{606}-I_{814}) = (V_{606}-I_{814})_{bulge} - (V_{606}-I_{814})_{passive}$$

In Table 2 we present $\langle\delta(V_{606}-I_{814})\rangle$, the *median* value of $\delta(V_{606}-I_{814})$, and the corresponding RMS dispersion, $\sigma_{\delta(V_{606}-I_{814})}$, for various subsamples of spiral bulge populations.

The distribution for the main sample (i.e. that plotted in Figure 4) is compared with that for the ellipticals in Figure 5 clearly illustrating the points made earlier. For this sample we obtain $\langle\delta(V_{606}-I_{814})\rangle$=-0.525 and $\sigma_{\delta(V_{606}-I_{814})}$=0.266. The median colors are substantially bluer than their elliptical counterparts, and it is apparent they fill in the regime between the passive elliptical population and the bluest elliptical outliers. Particularly striking is the almost complete absence of systems as red as the passive-evolution track which provides such a good description for the majority of the early-type population.

Two important conclusions can be drawn from Figure 4 and Table 2. Firstly, as described in the §3.2, we estimate typical contamination of bulge colors from disk light to be $V_{606}-I_{814} \lesssim 0.15$ mag for most early—intermediate spirals at redshifts $z < 0.5$. The median offset for the main sample given in Table 2 is therefore substantially larger ($\simeq \times 3$) than the expected RMS disk contamination for the galaxies in our spiral sample in this redshift range. At higher redshifts the significance of the blue bulge colors is hard to determine from optical data, but Figure 3 suggests that around a third of the spirals earlier than type Sbc at $z < 0.7$ should show little disk contamination ($V_{606}-I_{814}$ offsets less than 0.1 mag), although the optical colors of some systems will be significantly contaminated.

Secondly, in Table 2, the $\langle\delta(V_{606}-I_{814})\rangle$ color offsets and dispersions remain similar to the fiducial values for our main sample even if broadly different selection criteria are used to define the galaxy subsamples. Similar results are obtained when we: (a) restrict consideration only to large systems where the methodology is expected to be most effective; (b) restrict consideration only to low-inclination ($\frac{b}{a} > 0.5$) systems; (c) restrict consideration only to subsets of galaxies with confirmed spectroscopic redshifts. *The conclusions that most bulges are systematically bluer than the reddest ellipticals with a wide dispersion of colors is true regardless of the detailed prescription used to define the spiral subsamples.*

5. INTERPRETATION

Our principal result is that bulges are, statistically, optically bluer than the reddest ellipticals and show a large dispersion in their rest-frame colors. This result is insensitive to disk contamination, certainly for $z < 0.5$ and probably to higher redshifts since only a very small proportion (<5%) of intermediate redshift bulges have colors as red as those ellipticals with occupy a typical passively-evolving track defined according to a single burst of star formation at high redshift.

In considering the interpretation of these results in this section, we must take great care to distinguish between three reasonable working definitions for the age of a bulge component: (i) optical *luminosity-weighted age*, (ii) *structural age* (corresponding to the epoch at which the bulge component is formed morphologically), and finally (iii) the *age of the oldest stellar population* in the bulge. In the context of our observations these are not merely semantic distinctions — in fact understanding which of these ages is being probed by various aspects of our data is central to linking our observations with the predictions of theoretical models.

Our results clearly indicate that the optical luminosity-weighted ages of bulges to *at least* $z = 0.5$ are younger than those of the reddest ellipticals. Restriction of our sample to more robust (e.g. face-on) sub-samples does not change the strength of this conclusion. The pixel-by-pixel color distributions of representative spirals presented in Figure 2 gives a clear illustration of the overall result.

5.1. *Constraints on Secular Models*

We now consider the implications of younger luminosity-weighted ages for bulges from the viewpoint of models where bulges grow through secular evolution (Combes 1999). The paucity of bulges seen with optical colors close to the evolutionary track for a single burst of star formation seriously constrains a dominant population of old passively-evolving bulges. Similarly, the optical data is hard to reconcile with the notion that bulge formation proceeds secularly within the disk *without* associated star-formation in early–intermediate-type spirals. Further constraints on the secular picture depend upon whether the star-formation we infer from blue colors is associated with the formation epoch of the bulge itself, or with "pollution" by young stars upon a pre-existing, older, and morphologically established bulge component.

In the extreme case, if we assume that the blue colors are associated with the initial formation of the bulge, then conceivably *some* bulges formed at low redshift from the secular evolution of stellar disks with bars as an intermediate stage. Ellipticals could still form continuously from the merger of young disks at high redshift in which case their predominantly red colors in the redshift range $0< z <1$ would be compatible with growth in a low density or Λ-dominated cosmology (Kauffmann & Charlot 1998, Menanteau et al 1999, 2000). Given the small proportion of bulges as red as ellipticals in our redshift range, most bulges would have to have formed surprisingly recently and one would then expect a significant population of barred spiral precursors at higher redshift in contrast to the observations (Abraham et al 1999a). Interestingly, there is some evidence (c.f. Figure 2) that when bars are present, they do have redder colors than those of their bulges they contain as expected in the secular picture. However, numerically it seems unlikely that most present day bulges were formed in this way unless the number of $z >0.5$ barred systems has been seriously underestimated (c.f. Bunker 1999), or bulge formation is episodic, as

suggested by Sellwood (1999).

5.2. *Constraints on Hierarchical Models*

Next we proceed to discuss the implications of our results in the context of hierarchical galaxy formation models. Figure 6 illustrates the difference in observed $V_{606}-I_{814}$ colors expected for ellipticals, spiral bulges, and S0 galaxies in the ΛCDM semi-analytical prescription of Baugh et al. (in preparation), as a function of both redshift and apparent magnitude. Contrary to what is observed, the hierarchical picture predicts a much tighter color distribution for both bulges and ellipticals with the former being $\simeq$0.1-0.2 mag redder than ellipticals at high redshifts, and roughly similar colors at low redshift $z \lesssim 0.4$. In contrast to these predictions, we find that at $z < 0.5$ (ie. where possible systematic effects introduced by disk contamination can be neglected) bulges are significantly bluer than ellipticals.

Whilst suggestive of a major shortcoming in the predictions of the hierarchical model, the severity of this failure depends once again on whether the luminosity-weighted ages probed can be associated with the true formation epoch. An interpretation of our data broadly consistent with the hierarchical framework would be that most bulges are indeed produced from minor mergers of earlier disk systems (and hence that the underlying stellar populations in bulges are older than ellipticals) but that other physical effects that are missing from the models also play an important role in stimulating central star-formation after the bulk of the bulge mass is already in place (eg. secular processes that stimulate a modest amount of ongoing star formation in the central regions).

Although our observations do not necessarily require a major revision of the merger-driven astrophysics underlying the hierarchical models, a significant puzzle is the greater scatter in the colors of bulges compared to those in ellipticals (for which similar merger-driven activities are presumably occurring). The observed differences *might* be understood in terms of the timescales involved (see discussion below), as well as by the preferential morphological selection of ellipticals as relaxed remnants (Menanteau et al 1999).

5.3. *Models Incorporating Secondary Star Formation*

The discussion in §5.1 and §5.2 suggests that the major issue for understanding the ramifications of our optical observations for *both* secular and hierarchical models is the relationship between the luminosity-weighted ages of bulges and their structural ages. The key to establishing this would seem to be the measurement of the third "age measure" referred to earlier: namely establishing the epoch of formation and mass associated with the *initial* bulge-formation event.

In Figure 4 we show optical color-redshift trajectories for passively-evolving stellar populations upon which we have superposed 15% of the stellar mass, either in the form of a short-lived starburst or as an extended star-formation episode (modeled as exponential star-formation with a 5 Gyr e-folding timescale). The latter star-formation activity may be associated with a quasi-continuous infall of gas. We illustrate models corresponding to the onset of star-formation activity at redshifts $z = 0.2, 0.4, 0.6, 0.8,$ and 1.0.

A notable feature of the optical data is the bimodal nature of the deviations from the quiescent evolution track exhibited by the early-type galaxy population. Starburst models do not remain blue for much longer than the time associated with the active star-formation phase. At high redshifts, our observations probe sufficiently far into the ultraviolet that the observed V-band flux is dominated by current star-formation even for a moderate (10–15% by mass) burst. Unsurprisingly a "drip-feed" scenario results in a weaker but longer-lived blue phase suggesting that our present data can be used to place crude constraints on the duty-cycle of star-formation activity for both the bulges and early-type galaxies in our sample. The locus of very blue early-type systems combined with a paucity of intermediate-color early-type systems suggests that star-formation in high-redshift ellipticals is associated with rapid bursts whereas the broader color distribution observed for the bulges may be suggestive of a low-level, more extended star-formation.

As a quantitative example of the last point, consider two simple models: a passively evolving 5 Gyr old stellar population with roughly constant star-formation which then suffers a relatively minor nuclear starburst, and a pure starburst model with no underlying old stellar population. To be definitive, assume the starburst has an exponential star-formation history with an e-folding timescale of 100 Myr, and forms 10% of the mass of the underlying old population in the first model. Immediately after the burst phase, the composite (old + young) stellar population model at $z = 1$ is only 0.12 mag redder in $V-I$ than the pure burst model — at high redshifts, the young stellar population effectively masks the presence of any underlying old population in optical bands. However, the corresponding figure for $I-H$ is 0.51 mag. Extending the present methodology to the infrared allows one to determine, *in an individual case*, whether a blue bulge is associated with initial bulge formation or incremental bulge growth.

5.4. *Constraints from NICMOS Observations*

To make further progress we now turn to the resolved near-infrared (IR) data made possible through NICMOS observations of the HDF-North. As stated earlier, analysis of these data proceeded in the same manner as the analysis of drizzled WF/PC2 optical data. However, because the sampling of the NICMOS data is relatively poor, care is needed to ensure precise co-registration of the optical and IR data. Prior to our analysis all optical data was first convolved with the H_{160}-band PSF and re-binned to match the characteristics of the NIC3 dataset. The entire analysis process described earlier was then repeated for the convolved and rebinned optical data as well as for the NICMOS data (using, once again, the I_{814}-band images to define all central apertures). In order to test whether the coarser resolution of the NIC3 data was a major source of error, we constructed a new version of Figure 4 using the convolved and resampled V_{606} and I_{814} images, and found that the trends remained similar.

Even though only half our sample has been imaged (and with coarser resolution) with HST in the infrared, the benefits NICMOS offers are considerable. Firstly, disk contamination is expected to be less important at longer wavelengths, so if we see the same trends as in Figure 4, then this provides very strong confirmation of differences in the evolutionary behaviour of bulges and ellipticals as discussed above. Secondly, the addition of the IR photometry can break some of the degeneracy in the modelling based on optical colors discussed above since stars of different main sequence timescales are involved. As emphasized earlier, these advantages are offset by the poorer angular resolution and sensitivity of the NICMOS data (as well as by possible uncertainties in the modelling of stellar popula-

tion changes at near-IR wavelengths, as described by Charlot, Worthey, & Bressan 1996).

Figure 7 shows the $J_{110}-H_{160}$ color-redshift relation for the HDF-N targets plotted in Figure 4 with deep IR imaging. The model tracks discussed earlier in the context of Figure 4 are also plotted for the IR photometric bands. As mentioned, the IR models are mainly used to indicate general trends and we have displaced the $J_{110}-H_{160}$ BC96 model plotted in Figure 7 by +0.1 mag in order to ensure the passive evolution track lies closer to the locus defined by the redder E/S0 systems. We note that a $J_{110}-H_{160}=0.1$ mag color offset is quite compatible with the systematic effects seen by Charlot, Worthey, & Bressan 1996, who investigated the agreement in the predictions of independently-derived infrared models. Despite these caveats, the qualitative benefit of IR models is clear; timescales for synchronization of colours following a burst are much shorter in the IR and, unlike the case with optical colours, there is a very significant difference in the size of the color excursions arising from secondary star formation depending upon whether the bursts are intense and short-lived or of a gradual "drip-feed" nature.

With only half the HDF galaxies available, small number statistics become a significant complication, and consequently we remain cautious regarding the interpretation of the IR sample. However the general impression from a comparison of Figures 4 and 7 is that the optical/IR trends are very similar to intermediate redshifts ($z \lesssim 0.6$) but become somewhat different at high redshift ($z \gtrsim 0.6$). At intermediate redshifts, in both Figures 4 and 7 a dominant red E/S0 locus can be identified, although a minority of the E/S0 population lies well blueward of the overall relation. Clearly the photometric error is larger in the IR data. Furthermore, for $z \lesssim 0.6$, most of the spiral bulges have optical and IR colors intermediate between these extreme cases. However, at high redshifts, a significant fraction of *infrared* bulges now lie alongside the red ellipticals, and these are largely those in high central concentration spirals (large open symbols). Indeed many $z \gtrsim 0.6$ bulges appear to be slightly *redder* than their elliptical counterparts.

Assuming (as justified earlier) that disk contamination does not significantly complicate the interpretation of Figure 4 (§3.2) to redshifts $z \simeq 0.5$ and that this is completely negligible at all redshifts in Figure 7, then the combined data suggest that bulge building activity at higher redshifts is likely to be predominantly operating in a "short-burst" mode, rather than as part of a more extended "drip feed" process. Comparison with the model tracks suggests that the more extended recovery timescale for optical colors following a low-mass, short burst could well result in the majority of $z \gtrsim 0.6$ bulges lying near the red locus in the IR while at while being significantly offset in optical color.

A more interesting interpretation, though tentative given the small samples involved, would arise if the transition in the bulge IR color distribution seen in Figure 7 at or around $z \simeq 0.6$ is significant. This might imply that optically blue bulges are more common at $z \lesssim 0.6$ than at $z \gtrsim 0.6$ which could be understood if this redshift corresponded to one where a fundamental change in the bulge-building history of spirals occurred. This epoch has been claimed to be that at which barred spiral systems become fairly common in deep imaging data (Abraham et al. 1999). An increase in the fraction of blue bulges at this redshift could provide further evidence that the formation of Hubble's "tuning fork" occurs at or around this epoch, assuming the excess of $z < 0.6$ blue bulges corresponds to the onset of secular bulge-building processes. This would strengthen the link between bar formation and bulge-building (either through bar-driven gas flows or bar dissolution). It is perhaps interesting that a greater proportion of blue bulges at $z \lesssim 0.6$ occur in low central concentration galaxies than is the case at $z \gtrsim 0.6$, since the importance of secular activity is probably a strong function of Hubble type, as described earlier.

5.5. *Future Work*

The statistical relationship between bulge color and bulge-to-disk ratio as a function of redshift may also yield information on the epoch of initial bulge formation. If the structural parameters of the bulge can be reliably disentangled from the underlying disk, then high-redshift data that probes *in situ* formation from a structural standpoint can be used to isolate the epoch of bulge formation independently from the age of its stars. Such a study would also allow us to extend the present work in a number of interesting ways. In the present paper we have effectively decoupled measures of galactic structure from measures of stellar population, and hence we are unable to address quantitatively the important question of whether the enhanced blue colors of spiral bulges are associated with position on the Hubble sequence. Since the best evidence from local data is that secular activity is most closely associated with late-type spirals, studies linking the relative colors of bulges and ellipticals with measures of growth in bulge-to-disk ratio are required. Secular growth can also be examined directly in high-redshift galaxy data by kinematical observations that will soon become feasible with intermediate resolution spectrographs on 10m-class telescopes. Such dynamical data can be used to determine whether the bulk motions of high-redshift bulges have a closer kinematical connection to disk rotation or to thermal motions.

Coupling the present analysis to structural bulge-to-disk decompositions will also allow investigations of the extent to which the relatively blue bulges seen in our data may be the manifestation of a colour-magnitude relation (CMR) in field ellipticals, similar to that seen in well-studied cluster samples (Sandage & Visvanathan 1978). No CMR relation was found in high redshift HDF field ellipticals by Kodama, Bower, & Bell (1999), although its presence may have been masked by uncertainties arising from poorly-understood photometric redshifts.

Assuming that the slope of the field CMR at high redshifts resembles that seen in local cluster data, then the CMR has a completely negligible impact on our infrared bulge colors, and on the optical colors at $z < 0.5$. For example, the slope of the $B-R$ CMR in Coma is < 0.03 mag^{-1} (Milvang-Jensen & Jorgensen 2000), and presumably the $V-R$ slope is even smaller. At higher redshifts, where the I_{814} filter enters the rest-frame V-band, the CMR may begin to make optical bulge colors measurably bluer, although the effect probably represents a relatively small contribution to the systematic error budget. For example, in order for a Coma-like CMR to explain the whole of the present trend for blue bulges would require the bulges in our sample to be 6–8 mag fainter than typical ellipticals (assuming a Coma-like CMR of $\Delta(B-V)$=0.05 mag^{-1}), which is clearly incompatible with our visual pre-selection isolating relatively early-type spirals with large bulge-to-disk ratios. Furthermore a CMR is already incorporated into the hierarchical predictions given in Figure 6. Nevertheless, it will be interesting to compare the absolute magnitudes of the bulges in the present sample with the corresponding absolute magnitudes for ellipticals at similar redshifts, in order to establish the extent to which

cluster CMR data can be extended to spiral bulges in the field.

It is notable that the trends shown in Figures 4 and 7 are also seen when 5% apertures (instead of total apertures) are used to define the colors of the E/S0 population. This is not surprising, since Appendix 1 of Menanteau et al. (1999) indicates that the mean metallicity of an elliptical interior to its effective radius is reasonably close to the metallicity at the effective radius. This calculation is also illuminating when assessing the possible importance of metallicity gradients in biasing of the colors of spiral bulges. If the metallicity gradients in bulges are similar in strength to those in the luminous ellipticals studied by Arimoto et al. (1997), then the very slow drop-off in the mean metallicity of light interior to an aperture larger than the bulge effective radius implies that our 5% apertures should constitute a fair sample of the total bulge light.

Finally, we seek reassurance that the models outlined in Figures 4 and 7 are consistent with the colors and scatter observed locally for bulges and ellipticals. Surprisingly, however, there is no precise measure of the local homogeneity of bulges (Wyse et al 1997). Peletier et al (1999), in a particularly detailed optical-infrared analysis of 20 nearby systems with HST, draw attention to the redder colors of the inner 100-200 pc some component of which they attribute to dust obscuration. (We note that the presence of nuclear dust at this level, if confirmed, would further strengthen the results of the present paper.) On scales corresponding to bulge effective radii, where dust effects are expected to be negligible, Peletier et al (1999) find mean bulge colors comparable to those of Coma ellipticals. However, imprecise photometric conversions were necessary to make this comparison, rendering the precision of this statement no better than ± 0.2 mag in $B-I$. The color dispersion in the bulges themselves is typically also $\simeq$0.15-0.2 mag in $B-I$. Clearly, improved local data are needed to establish the relative colors of bulges and ellipticals in the local Universe.

6. CONCLUSIONS

A robust prediction of hierarchical scenarios that associates morphological transformations with mergers and disk growth is that bulges must be statistically redder and older than ellipticals. In order to test this prediction, we have collated a magnitude limited sample of spirals and ellipticals from both Hubble Deep Fields and compared the aperture-based $V_{606}-I_{814}$ color-redshift relation for the central bulges of spirals selected in various ways with those of field ellipticals.

In detail we find the following:

- At $z \lesssim 0.6$, where we demonstrate that contamination from underlying disk light is minimal, bulges are significantly bluer than elliptical galaxies. Very few bulges follow traditionally-accepted passive evolutionary tracks. At optical wavelengths most bulges are 0.3-1.0 mag *bluer* than ellipticals at comparable redshifts, with a significant color dispersion at a given redshift, in marked contrast to the expectations of recent semi-analytic predictions. Statistically speaking, bulges remain optically bluer than ellipticals at all redshifts $z \gtrsim 0.6$ to the limits of our data, and contamination by bluer disk light and/or aperture mismatches is unlikely to explain the bulk of this effect.

- Although at first sight our data suggest that bulges are recently formed, we show that secondary star formation involving bursts of 15% by mass superimposed upon a pre-existing old stellar population can readily reproduce the color dispersion observed. We discuss two general scenarios: short-lived bursts and extended events possibly associated with continuous infall of gas.

- Near-infrared NICMOS observations of a sub-sample of our dataset agree with the optical trends at $z \lesssim 0.6$, but at higher redshifts most infrared bulges appear to be as red as most ellipticals. Model comparison with the optical trends suggests that the duty cycle for the optical blueing of high-redshift bulges is quite short. Most importantly, however, our data firmly rule out the traditional picture whereby bulges form at high redshift and evolve passively as miniature ellipticals. Although somewhat speculative at this stage, the divergence observed in the IR properties of bulges and ellipticals at $z \sim 0.6$ may suggest that other physical processes become important in forming galactic bulges, for example secular evolution in stellar disks linked to the formation of galactic bars.

- Much work needs to be done at both high and low redshifts in order to establish the star-formation history of bulges in various galaxy types and their environments. It is clear that such studies are central to testing hierarchical models for the morphological evolution of galaxies. In this paper we have shown significant differences between the distribution of colors in bulges and ellipticals which either seriously challenge our theoretical views on bulge formation or, more likely, reveal the necessity for including additional physics into these models, corresponding to periods of extended star formation in the inner regions of spiral galaxies.

7. ACKNOWLEDGEMENTS

We thank Carlton Baugh, Shaun Cole and Carlos Frenk for their enthusiastic support of this project and Carlton Baugh for generously giving us semi-analytic predictions in the context of our observations. We thank Stephen Gwyn for kindly making his photometric catalog available to us, and for matching the object identifications in his catalog to those given in the STScI HDF catalog. Reynier Peletier is thanked for making the results from his NICMOS bulge progam known to us in advance of publication. We acknowledge useful discussions with Jarle Brinchmann, Ray Carlberg, Roger Davies, Gerry Gilmore, Piero Madau, Ron Marzke, Felipe Menanteau, Mike Merrifield, Rachel Somerville and Chuck Steidel.

REFERENCES

Abraham, R. G., Tanvir, N. R., Santiago, B. X., Ellis, R. S., Glazebrook, K. & van den Bergh, S. 1996, MNRAS, 279, L47

Abraham, R.G., Merrifield, M., Ellis, R.S., Tanvir, N.R. & Brinchmann, J. 1999a *Mon. Not. R. astr. Soc.* in press (astro-ph/9811476).

Abraham, R.G., Ellis, R.S., Fabian, A.C., Tanvir, N.R. & Glazebrook, K. 1999b *Mon. Not. R. astr. Soc.*, **303**, 641.

Andredakis, Y. C. & Sanders, R. H. 1994, *Mon. Not. R. astr. Soc.*, **267**, 283.

Arimoto, N., Matsushita, K., Ishimaru, Y., Ohashi, T., & Renzini, A. 1997, ApJ, 477, 128

Baugh, C.M., Cole, S., Frenk, C.S., Lacey, C.G. 1998 *Astrophys. J.*, **498**, 504.

Bower, R.G., Kodama, T. & Terlevich, A. 1998 *Mon. Not. R. astr. Soc.*, **299**, 1193.

Brinchmann, J., Abraham, R.G., Schade, D.J., Tresse, L., Ellis, R.S., Lilly, S.J., LeFevre, O., Glazebrook, K., Hammer, F. & Colless, M. 1998 *Astrophys. J.*, **499**, 112.
Bunker, A. in *The OCIW Workshop on Photometric Redshifts*, ed. Weymann, R. et al, in press (astro-ph/9907196).
Charlot, S. & Bruzual, G. 1999, in preparation.
Combes, F. 1999 preprint (astro-ph/9904031)
de Jong, R. 1996 *Astr. Astrophys.*, **313**, 377.
Dickinson, M.E. 2000 in *Building Galaxies: From the Primordial Universe to the Present*, XIXth Moriond Astrophysics Meeting, eds. Hammer, F. et al, (Paris:Ed. Frontieres), p257.
Driver, S., Windhorst, R.A. & Griffiths, R.E. 1995 *Astrophys. J.*, **453**, 48.
Dwek, E. et al 1995 *Astrophys. J.* **445**, 716.
Eggen, O.J., Lynden-Bell, D. & Sandage, A. 1962 *Astrophys. J.*, **136**, 748.
Frankston, M., & Schild, R. (1976), *Astron. J.*, **81**, 500
Kauffmann, G., White, S.D.M. & Guiderdoni, B. 1993 *Mon. Not. R. astr. Soc.*, **264**, 201.
Kauffmann, G. & Charlot, S. 1998 *Mon. Not. R. astr. Soc.*, **297**, L23.
Kodama, T., Bower, R.G. & Bell, E.F. 1999 *Mon. Not. R. astr. Soc.*, (in press).
Kormendy, J. 1993, in *Galactic Bulges*, eds. Dejonghe, H. and Jabing, H. J, Kluwer Academic Publishshers, p.209-228
Kuijken, K. & Merrifield, M. 1995 *Mon. Not. R. astr. Soc.*, **443**, L13.
Lilly, S.J., Schade, D.J., Ellis, R.S., LeFevre, O., Brinchmann, J., Abraham, R.G., Tresse, L., Hammer, F., Crampton, D., Colless, M. & Glazebrook, K. 1998 *Astrophys. J.*, **500**, 75.
Marleau, F. & Simard, L. 1998 *Astrophys. J.*, **507**, 585.
Marzke, R.O. et al. 1994 *Astron. J.*, **108**, 437.
Menanteau, F., Ellis, R.S., Abraham, R.G., Barger, A. & Cowie, L. 1999a *Mon. Not. R. astr. Soc.*, in press (astro-ph/9811465)
Menanteau, F., Abraham, R.G. & Ellis, R.S. (2000), in preparation.
Milvang-Jensen, B. & Jorgensen, I. (2000); astro-ph/0004049
Norman, C., Sellwood, J. & Hasan, H. 1996 *Astrophys. J.*, **462**, 114.
Peletier, R.F., Balcells, M., Davies, R.L., Andredakis, Y., Vazdekis, A., Burkers, A. & Prada, F. 1999 *Mon. Not. R. astr. Soc.*, submitted.
Ratnatunga, K.U., Griffiths, R.E. & Ostrander, E.J. 1999 *Astron. J.*, in press (astro-ph/9904179)
Rich, M. 1997 in *The Central Regions of the Galaxy and Galaxies*, IAU Symposium 184, Kluwer.
Schade, D.J., Lilly, S.J., Crampton, D. et al 1995, *Astrophys. J.*, **451**, L1.
Schade, D.J., Crampton, D., Hammer, F., LeFevre, O. & Lilly, S.J. 1996 *Mon. Not. R. astr. Soc.*, **278**, 95.
Schade, D.J., Lilly, S.J., Crampton, D., Ellis, R.S., LeFevre,O., Hammer, F., Brinchmann, J., Abraham, R.G., Colless, M. & Tresse, L. 1999 *Astrophys. J.*, in press (astro-ph/9906171).
Sellwood, J. 1999 in *Galaxy Dynamics*, eds. Merritt, M. et al, in press (astro-ph/9904084)
van den Bergh, S. 1998, “Galaxy Morphology and Classification”, (Cambridge: Cambridge University Press).
Williams, R. et al 1996 *Astron. J.*, **112**, 1335.
Williams, R. et al 1999 in preparation.
Wyse, R.F.G., Gilmore, G. & Franx, M. 1997 *Ann. Rev. Astron. Astrophys.*, **35**, 637.

FIG. 1.— **SEE JPEG IMAGE: F1.JPG**. I_{814}-band images of all non-peculiar, non-blended spirals in our sample (Plate 1). The small yellow central aperture shown on each galaxy is used to determine the bulge color as described in the text. Redshifts and elliptical-aperture-based total I_{814}-band magnitudes are shown on each panel. Photometric redshifts are shown in parentheses.

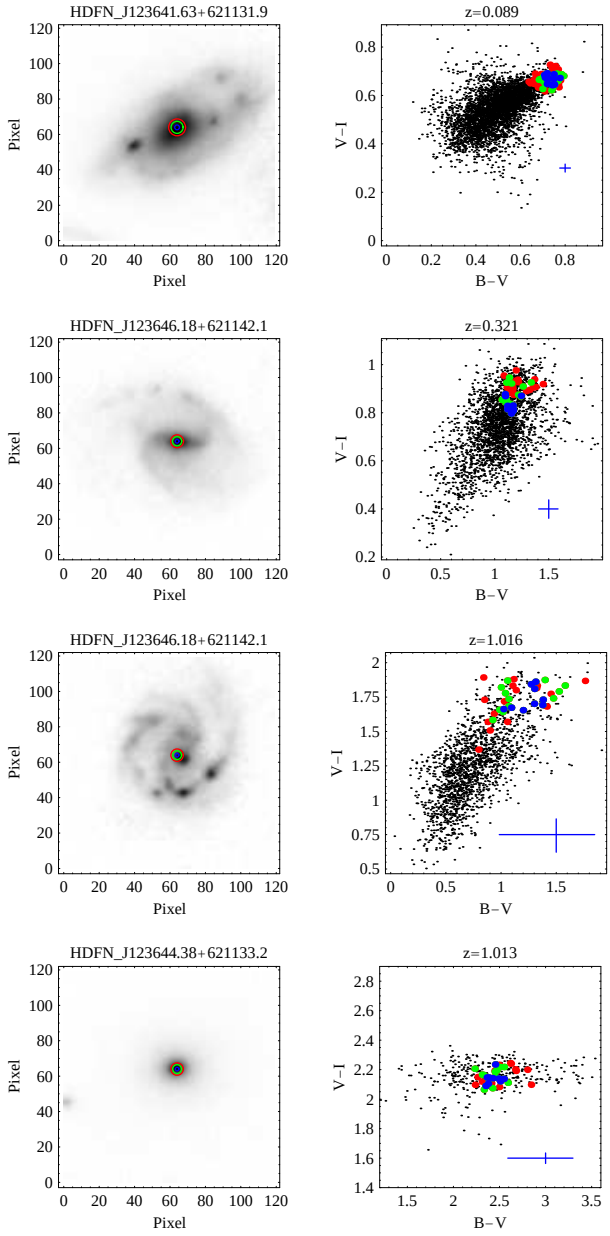

FIG. 2.— [Left] I_{814}-band images of three bright spirals and one elliptical from our sample. Circles correspond to fractional radial apertures of 2% (blue), 5% (green) and 7% (red) of the semi-major axis length of the galaxy. [Right] Corresponding pixel-by-pixel color-color distributions. Pixels internal to the circular apertures on the left-hand panels are shown with the same color coding. The error bars shown correspond to those for typical pixels in the 2% apertures.

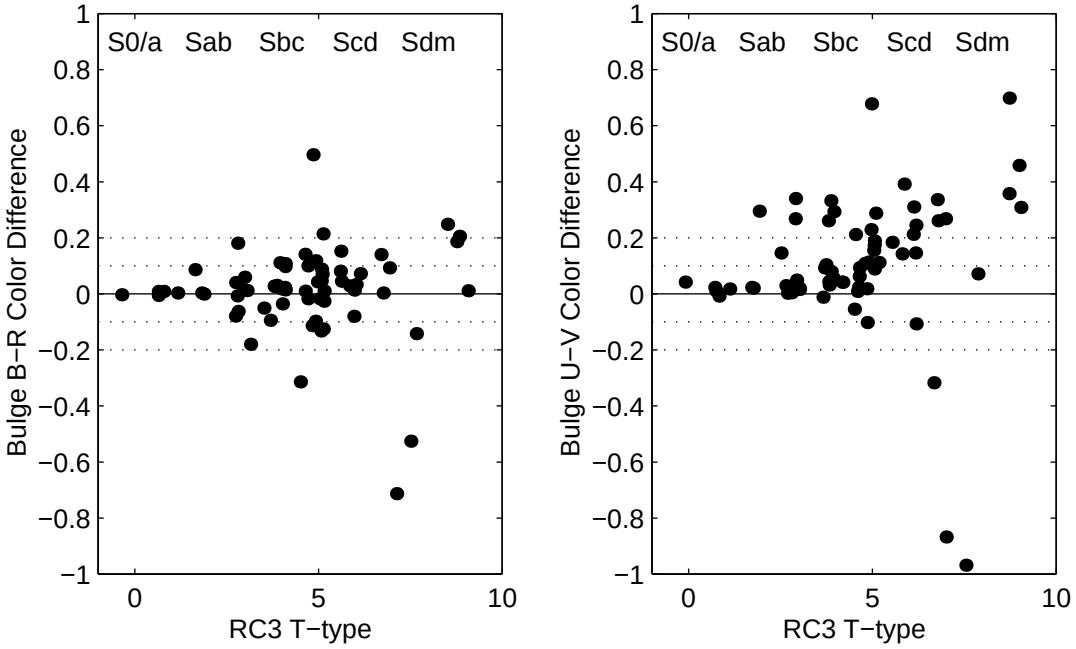

FIG. 3.— The difference between bulge colors determined using the simple aperture-based procedure described in the text and bulge colors determined using two-dimensional fits to galaxy surface brightness distributions, for the nearby sample of spirals of de Jong (1996). Color differences are shown as a function of Hubble sequence T-type from the *Third Reference Catalog*. For clarity, T-types are plotted with small random offsets. The difference between the estimated $B-R$ and $U-V$ bulge colors are shown in the left and right panels, respectively. As described in the text, these approximate to the rest-frame colors corresponding to $V_{606}-I_{814}$ at redshifts of 0.4 and 0.7, respectively.

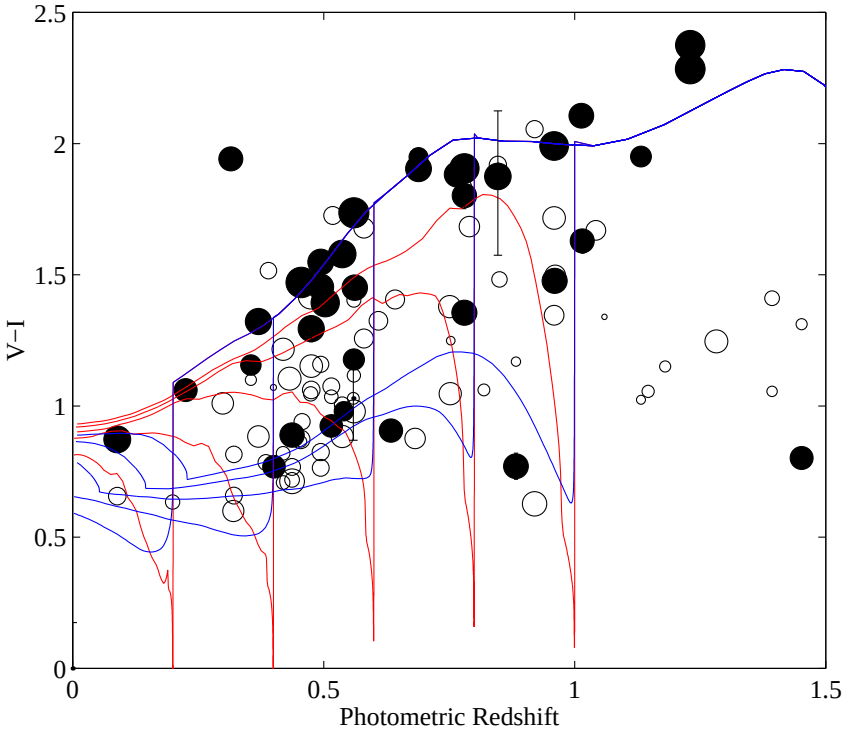

FIG. 4.— $V_{606}-I_{814}$ colors for ellipticals (solid symbols, large aperture) and spiral bulges (open symbols, 5% aperture - see text) as a function of photometric redshift. The spiral sample was defined according to the entries in Table 1 with RGA=Sab|Sbc|Disc, blend=no|minor, bulge=yes, pec=no. Symbol sizes are proportional to galactic central concentration, as defined in Abraham et al. (1996). Representative error bars are shown on several data points. Note the striking offset in the colors of spiral bulges relative to the red elliptical locus at any given redshift. This offset is much larger than the expected contribution from blue disk light shown in Figure 3. The solid blue curve at the top represents the observed $V_{606}-I_{814}$ color expected for a passively-evolving system that formed in a single burst at z=3. This is the baseline model upon which secondary bursts are added. The other curves define color-redshift trajectories for systems which suffer secondary bursts of activity at redshifts of 0.2,0.4,0.6,0.8 and 1. Red curves refer to 0.1 Gyr bursts involving 15% of the stellar mass whereas the blue curves refer to extended bursts with 5 Gyr e-folding timescales (see §5.3 in the text for details).

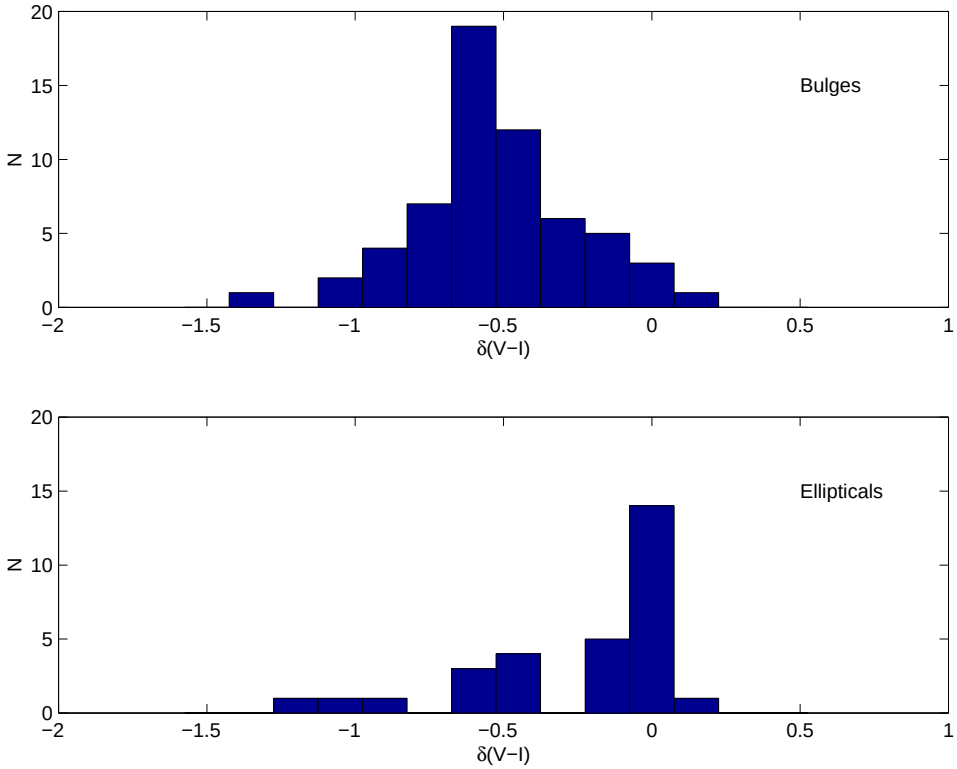

FIG. 5.— The distribution of $V_{606}-I_{814}$ colors for the spiral bulges and ellipticals plotted in Figure 4 with respect to the passive evolutionary prediction. Although these color differences span similar ranges in the observer's frame, the distributions are quite different with the elliptical distribution showing bimodal characteristics.

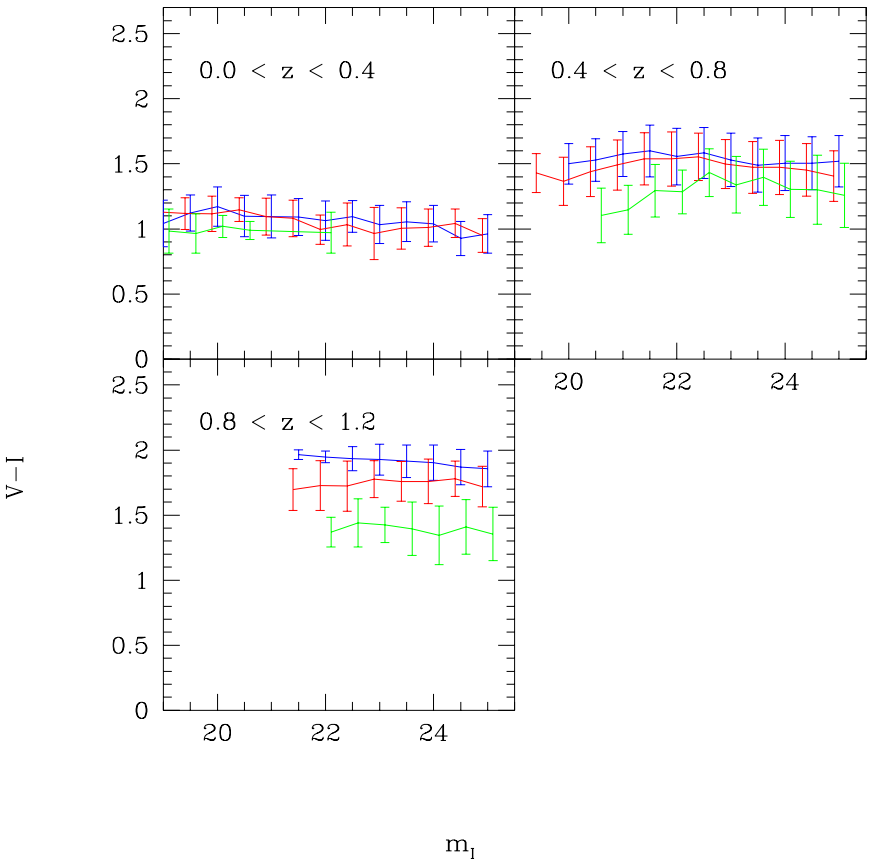

FIG. 6.— The predicted colors (courtesy of Carlton Baugh) of bulges, ellipticals, and S0 galaxies in three broad redshift bins: $0 < z < 0.4$ (top left), $0.4 < z < 0.8$ (top right), and $0.8 < z < 1.2$ (lower left) based upon the semi-analytical prescription of Baugh et al. (1999). $V_{606} - I_{814}$ color versus total galaxy I_{814} magnitude is shown for spiral bulges (blue), ellipticals (red) and S0 galaxies (green). Mean colors are joined by solid lines, and error bars correspond to the color variance.

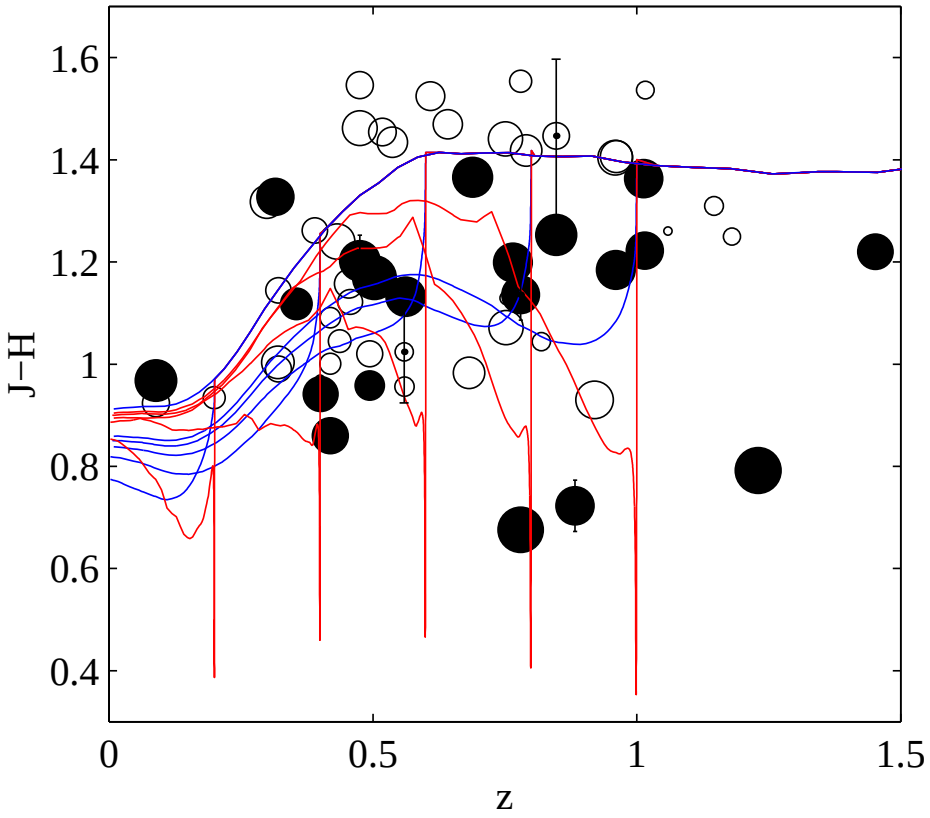

FIG. 7.— Infrared J-H color redshift distribution for the HDF sample of bulges and ellipticals adopted in Figure 4 with the same symbols and model predictions (see text for details).

This figure "f1.jpg" is available in "jpg" format from:

http://arXiv.org/ps/astro-ph/0010401v1

Table 1. HDF North and South Sample

ID[a]	I_{814}[b]	H_{160}[c]	z[d]	$V-I$[e]	$V-I$[f]	$J-H$[g]	$J-H$[h]	ϵ[i]	C[j]	A[k]	Auto[l]	RSE[m]	
HDFN_J123649.44+621346.9	18.19	16.10	0.089	0.86	0.87	1.22	0.97	0.33	0.68	0.06	Early	0	
HDFS_J223254.90-603144.1	18.75	···	-1.000	1.86	1.84	···	···	0.08	0.90	0.20	Star	-2	
HDFS_J223305.04-603400.8	19.18	···	-1.000	1.71	1.64	···	···	0.09	0.89	0.30	Star	-2	
HDFN_J123656.35+621241.2	19.20	17.03	-1.000	0.58	0.68	0.72	0.83	0.19	0.90	0.14	Star	-2	
HDFN_J123654.73+621328.0	19.31	17.17	-1.000	0.82	1.14	1.07	0.90	0.04	0.92	0.32	Star	-2	
HDFS_J223247.66-603335.9	19.55	···	0.580	1.68	1.26	···	···	0.36	0.44	0.11	Spiral	5	
HDFN_J123651.06+621320.7	19.62	18.01	0.199	0.63	0.56	0.93	0.86	0.26	0.30	0.16	Pec	5	
HDFN_J123641.63+621131.9	19.80	18.09	0.089	0.66	0.53	0.92	0.89	0.40	0.37	0.17	Spiral	4	
HDFS_J223250.51-603218.8	19.85	···	-1.000	1.15	0.79	···	···	0.11	0.91	0.20	Star	-2	
HDFS_J223247.45-603160.0	19.85	···	-1.000	2.56	2.65	···	···	0.13	0.90	0.10	Star	-2	
HDFN_J123656.64+621245.5	19.98	17.62	0.518	1.73	1.44	1.45	1.23	0.52	0.39	0.05	Spiral	2	
HDFS_J223303.58-603341.7	20.07	···	(0.419)	1.22	1.01	···	···	0.20	0.51	0.05	Early	5	
HDFS_J223303.65-603330.6	20.23	···	-1.000	1.88	1.97	···	···	0.08	0.91	0.38	Star	-2	
HDFS_J223302.76-603322.1	20.34	···	(0.474)	1.42	1.29	···	···	0.46	0.59	0.07	Early	3	
HDFN_J123648.08+621309.0	20.43	18.05	0.475	1.46	1.29	1.37	1.20	0.13	0.64	0.09	Early	0	
HDFS_J223257.54-603306.1	20.45	···	0.580	1.26	1.02	···	···	0.04	0.42	0.13	Spiral	3	
HDFN_J123650.22+621239.8	20.67	18.79	0.474	0.79	0.84	1.17	0.98	0.37	0.45	0.29	Spiral	8	
HDFN_J123642.92+621216.4	20.75	18.72	0.454	0.87	0.85	1.16	1.01	0.08	0.41	0.15	Spiral	4	
HDFN_J123652.82+621432.1	20.84	19.26	-1.000	0.50	0.74	0.88	0.79	0.14	0.88	0.19	Star	-2	
HDFN_J123643.81+621142.9	20.87	18.17	0.765	1.91	1.88	1.30	1.20	0.14	0.61	0.06	Early	0	
HDFN_J123653.90+621254.0	20.89	18.48	0.642	1.41	1.28	1.47	1.23	0.22	0.42	0.12	Spiral	4	
HDFS_J223250.90-603243.0	20.90	···	(0.494)	1.50	1.45	···	···	0.08	0.64	0.11	Early	0	
HDFN_J123643.97+621250.1	20.94	18.68	0.557	1.12	1.10	1.47	1.23	0.52	0.46	0.15	Spiral	6	
HDFN_J123648.33+621249.8	20.98	18.44	-1.000	2.02	2.15	1.10	0.94	0.04	0.85	0.34	Star	-2	
HDFN_J123641.95+621205.4	20.98	18.83	0.432	1.10	0.91	1.24	1.10	0.05	0.53	0.07	Early	3	
HDFS_J223252.29-603308.5	21.02	···	(0.560)	1.04	0.95	···	···	0.13	0.26	0.13	Pec	5	S
HDFN_J123647.05+621236.9	21.02	18.94	0.320	0.66	0.73	1.03	0.99	0.07	0.57	0.07	Early	2	
HDFS_J223253.92-603313.5	21.06	···	(0.225)	1.04	1.06	···	···	0.41	0.54	0.04	Early	2	

arXiv:astro-ph/0010401v1 19 Oct 2000

Table 1—Continued

ID[a]	I_{814}[b]	H_{160}[c]	z[d]	$V-I$[e]	$V-I$[f]	$J-H$[g]	$J-H$[h]	ϵ[i]	C[j]	A[k]	Auto[l]	RSE[m]	R
HDFN_J123645.42+621213.6	21.07	20.68	-1.000	-0.14	0.10	0.21	0.16	0.06	0.90	0.07	Star	-2	S
HDFN_J123651.80+621353.8	21.08	18.66	0.557	1.35	1.16	1.42	1.26	0.40	0.48	0.17	Spiral	7	
HDFN_J123658.75+621252.4	21.14	19.46	0.321	0.82	0.70	1.14	0.94	0.22	0.35	0.08	Spiral	5	
HDFS_J223253.64-603236.0	21.15	···	(0.313)	0.90	0.84	···	···	0.57	0.37	0.15	Spiral	7	
HDFS_J223247.58-603408.6	21.20	···	(0.583)	1.31	1.03	···	···	0.32	0.41	0.14	Spiral	3	
HDFS_J223254.68-603333.2	21.22	···	(0.161)	0.77	0.75	···	···	0.60	0.46	0.09	Spiral	5	I
HDFN_J123657.31+621259.7	21.22	19.00	0.474	0.66	0.74	1.06	1.09	0.36	0.36	0.23	Pec	4	
HDFN_J123653.66+621308.3	21.23	19.43	-1.000	0.97	0.99	0.90	0.82	0.17	0.90	0.21	Star	-2	S
HDFN_J123646.35+621404.7	21.23	18.54	0.960	0.92	1.48	1.17	1.18	0.26	0.61	0.07	Early	0	S
HDFS_J223256.07-603148.9	21.23	···	(0.474)	1.05	0.87	···	···	0.28	0.30	0.16	Pec	4	
HDFN_J123646.18+621142.1	21.27	18.51	1.016	1.60	1.28	1.54	1.23	0.13	0.25	0.21	Pec	4	
HDFS_J223246.90-603354.9	21.28	···	(0.537)	1.56	1.58	···	···	0.36	0.71	0.07	Early	2	E
HDFS_J223258.30-603351.7	21.35	···	(1.337)	2.40	2.50	···	···	0.02	0.80	0.17	Early	-1	
HDFN_J123700.56+621234.7	21.38	19.02	0.562	1.47	1.45	1.32	1.13	0.07	0.63	0.06	Early	0	E
HDFN_J123650.27+621245.8	21.40	18.77	0.680	1.80	1.69	1.38	1.23	0.28	0.56	0.06	Early	2	
HDFN_J123649.72+621313.0	21.42	19.04	0.475	1.06	1.08	1.55	1.30	0.64	0.38	0.17	Spiral	4	
HDFS_J223248.06-603148.6	21.46	···	-1.000	0.49	0.58	···	···	0.09	0.81	0.12	Star	0	S
HDFN_J123651.72+621220.3	21.48	19.26	0.299	1.01	0.97	1.32	1.19	0.53	0.49	0.17	Spiral	1	
HDFN_J123644.38+621133.2	21.50	17.82	1.013	2.14	2.11	1.44	1.36	0.17	0.60	0.05	Early	0	
HDFS_J223253.74-603337.6	21.53	···	(0.515)	1.04	0.85	···	···	0.06	0.28	0.08	Spiral	5	
HDFS_J223256.54-603152.8	21.55	···	-1.000	0.39	0.51	···	···	0.04	0.79	0.38	Early	-2	
HDFS_J223255.72-603211.5	21.57	···	(0.560)	1.71	1.73	···	···	0.39	0.60	0.08	Early	2	S
HDFS_J223248.47-603139.3	21.59	···	(0.959)	1.93	1.99	···	···	0.04	0.75	0.17	Early	0	
HDFN_J123644.19+621247.8	21.63	19.62	0.555	0.60	0.74	1.08	0.94	0.15	0.40	0.21	Spiral	7	
HDFS_J223252.71-603207.3	21.66	···	(0.437)	0.77	0.74	···	···	0.37	0.36	0.12	Spiral	3	
HDFS_J223254.78-603215.5	21.66	···	(0.494)	1.57	1.55	···	···	0.17	0.64	0.13	Early	0	
HDFS_J223251.03-603353.5	21.69	···	(1.452)	2.69	2.77	···	···	0.10	0.83	0.13	Early	-1	
HDFS_J223252.60-603259.5	21.69	···	-1.000	1.39	1.46	···	···	0.34	0.82	0.25	Star	-2	S

Table 1—Continued

ID[a]	I_{814}[b]	H_{160}[c]	z[d]	$V-I$[e]	$V-I$[f]	$J-H$[g]	$J-H$[h]	ϵ[i]	C[j]	A[k]	Auto[l]	RSE[m]	R
HDFS_J223301.89-603316.4	21.71	···	(0.370)	0.88	0.90	···	···	0.38	0.49	0.27	Spiral	2	
HDFN_J123643.16+621242.2	21.72	18.82	0.847	1.97	1.87	1.42	1.25	0.20	0.67	0.06	Early	1	
HDFN_J123649.51+621406.7	21.78	19.40	0.751	1.38	1.31	1.44	1.23	0.35	0.51	0.13	Spiral	1	
HDFS_J223252.14-603359.6	21.78	···	(0.560)	1.40	1.05	···	···	0.69	0.30	0.24	Pec	5	
HDFS_J223251.33-603237.6	21.79	···	(0.560)	1.60	1.74	···	···	0.10	0.81	0.19	Early	0	F
HDFS_J223247.58-603347.4	21.87	···	(0.455)	1.39	1.47	···	···	0.14	0.82	0.27	Early	-1	
HDFN_J123655.56+621245.6	21.89	19.74	0.790	1.68	1.27	1.42	1.16	0.14	0.46	0.09	Spiral	4	
HDFN_J123646.52+621151.3	21.97	19.59	0.503	1.34	1.39	1.36	1.17	0.13	0.74	0.16	Early	1	
HDFN_J123649.64+621257.6	21.98	19.53	0.475	1.15	1.03	1.46	1.25	0.45	0.53	0.23	Spiral	4	
HDFS_J223252.23-603402.8	21.98	···	(0.560)	0.98	1.15	···	···	0.49	0.53	0.07	Early	3	
HDFS_J223258.22-603331.6	21.99	···	(0.385)	0.78	0.77	···	···	0.24	0.33	0.11	Spiral	5	
HDFS_J223259.43-603339.8	22.00	···	(0.437)	0.92	0.84	···	···	0.21	0.28	0.24	Pec	6	
HDFN_J123649.38+621311.3	22.05	20.14	0.478	0.78	0.88	1.21	1.07	0.16	0.61	0.18	Early	1	
HDFS_J223251.51-603337.6	22.08	···	(0.560)	1.30	1.18	···	···	0.24	0.48	0.08	Spiral	7	S
HDFS_J223256.08-603414.2	22.09	···	(0.537)	0.88	0.89	···	···	0.35	0.51	0.06	Early	3	
HDFS_J223254.05-603251.7	22.12	···	(0.437)	0.71	0.83	···	···	0.32	0.60	0.09	Early	8	
HDFS_J223250.29-603203.3	22.16	···	(0.437)	0.81	0.89	···	···	0.06	0.59	0.07	Early	0	
HDFN_J123655.46+621311.2	22.17	18.93	0.315	2.03	1.94	1.43	1.33	0.10	0.57	0.03	Early	1	F
HDFN_J123638.98+621219.8	22.23	20.34	0.609	1.05	0.98	1.12	0.97	0.29	0.38	0.28	Pec	4	
HDFS_J223245.74-603309.7	22.25	···	(1.514)	2.74	2.83	···	···	0.16	0.64	0.25	Early	1	F
HDFS_J223302.45-603346.5	22.28	···	0.690	0.60	0.93	···	···	0.36	0.28	0.35	Pec	7	
HDFN_J123640.02+621207.4	22.28	19.53	1.015	1.78	1.63	1.31	1.22	0.04	0.58	0.08	Early	1	F
HDFN_J123658.06+621300.4	22.32	20.78	0.320	0.43	0.52	1.03	0.86	0.58	0.56	0.20	Spiral	4	
HDFN_J123646.14+621246.5	22.33	19.76	(0.780)	1.80	1.80	1.40	1.14	0.13	0.59	0.08	Early	1	F
HDFS_J223257.11-603152.1	22.36	···	(0.277)	1.08	0.90	···	···	0.40	0.41	0.20	Spiral	9	F
HDFN_J123646.77+621237.1	22.38	20.29	(0.560)	1.64	1.75	1.58	1.15	0.09	0.68	0.29	Early	0	
HDFS_J223256.05-603220.6	22.40	···	(0.515)	0.92	0.77	···	···	0.46	0.28	0.13	Pec	4	
HDFN_J123657.21+621225.9	22.41	20.72	0.561	1.05	0.85	1.13	1.01	0.21	0.27	0.19	Pec	8	

Table 1—Continued

ID[a]	I_{814}[b]	H_{160}[c]	z[d]	$V-I$[e]	$V-I$[f]	$J-H$[g]	$J-H$[h]	ϵ[i]	C[j]	A[k]	Auto[l]	RSE[m]	R
HDFS_J223249.23-603253.4	22.43	···	(0.560)	1.12	0.99	···	···	0.03	0.28	0.05	Spiral	3	
HDFS_J223301.77-603413.5	22.44	···	(0.920)	2.05	1.38	···	···	0.23	0.37	0.11	Spiral	5	
HDFN_J123654.10+621354.3	22.44	20.36	0.850	1.48	1.21	1.27	1.08	0.27	0.32	0.09	Spiral	4	
HDFN_J123643.19+621148.0	22.44	19.40	(0.847)	1.92	1.73	1.45	1.35	0.31	0.37	0.08	Spiral	4	
HDFN_J123650.17+621217.0	22.44	19.57	(1.000)	1.94	1.98	1.56	1.33	0.63	0.40	0.14	Spiral	4	
HDFN_J123659.30+621255.8	22.45	20.20	(1.230)	2.17	2.28	0.75	0.79	0.14	0.80	0.14	Early	0	
HDFN_J123649.06+621221.3	22.45	20.50	0.953	1.10	1.10	1.10	0.94	0.12	0.29	0.20	Pec	4	
HDFS_J223253.34-603239.3	22.46	···	(1.786)	1.43	1.22	···	···	0.38	0.30	0.20	Pec	7	
HDFS_J223256.68-603313.8	22.46	···	(1.230)	2.27	2.37	···	···	0.08	0.78	0.23	Early	0	I
HDFS_J223250.55-603325.9	22.51	···	(0.494)	1.15	1.06	···	···	0.24	0.31	0.05	Spiral	4	
HDFN_J123656.65+621220.2	22.53	19.54	(1.042)	2.04	1.88	1.44	1.30	0.19	0.53	0.09	Spiral	1	
HDFN_J123650.82+621255.9	22.54	20.96	0.320	0.60	0.53	1.00	0.91	0.55	0.48	0.07	Spiral	4	
HDFS_J223253.03-603328.5	22.57	···	(1.282)	1.25	1.39	···	···	0.10	0.53	0.08	Early	2	
HDFN_J123638.41+621231.4	22.58	20.12	(0.537)	1.53	1.28	1.53	1.30	0.67	0.31	0.25	Pec	4	I
HDFN_J123650.48+621316.1	22.62	20.07	(0.780)	1.84	1.44	1.55	1.34	0.63	0.30	0.09	Spiral	4	
HDFN_J123648.26+621213.9	22.63	20.34	(0.883)	1.43	1.26	1.26	1.02	0.31	0.22	0.16	Pec	8	
HDFN_J123652.78+621354.3	22.64	20.17	1.355	0.45	0.58	1.16	0.90	0.58	0.20	0.41	Pec	8	
HDFN_J123655.53+621353.4	22.65	20.59	1.146	1.06	0.87	1.31	1.05	0.07	0.26	0.13	Pec	4	
HDFS_J223252.06-603140.8	22.66	···	(0.494)	0.86	0.62	···	···	0.55	0.30	0.40	Pec	8	
HDFS_J223248.90-603404.8	22.67	···	(0.780)	1.07	1.36	···	···	0.01	0.61	0.14	Early	0	
HDFS_J223247.94-603216.6	22.69	···	(2.023)	0.58	0.73	···	···	0.12	0.74	0.19	Early	1	I
HDFN_J123641.32+621140.9	22.70	20.09	0.585	1.53	1.51	1.41	1.33	0.43	0.35	0.12	Spiral	4	I
HDFN_J123648.78+621318.5	22.70	21.03	0.753	1.25	1.05	1.13	0.90	0.21	0.21	0.13	Pec	8	
HDFN_J123654.04+621245.6	22.70	20.62	(0.780)	1.83	1.91	0.63	0.68	0.18	0.77	0.33	Early	-1	I
HDFN_J123643.63+621218.3	22.70	20.79	0.752	1.05	1.12	1.07	1.02	0.32	0.51	0.13	Spiral	1	
HDFS_J223254.02-603305.6	22.71	···	(0.494)	1.21	1.30	···	···	0.55	0.37	0.32	Pec	4	I
HDFS_J223252.35-603333.0	22.72	···	(0.515)	0.83	0.92	···	···	0.30	0.53	0.15	Spiral	0	S
HDFS_J223258.46-603307.7	22.74	···	(0.437)	1.22	1.32	···	···	0.08	0.68	0.12	Early	0	

Table 1—Continued

ID[a]	I_{814}[b]	H_{160}[c]	z[d]	$V-I$[e]	$V-I$[f]	$J-H$[g]	$J-H$[h]	ϵ[i]	C[j]	A[k]	Auto[l]	RSE[m]	
HDFN_J123651.43+621300.7	22.75	21.88	0.089	0.58	0.37	0.98	0.63	0.19	0.24	0.19	Pec	8	S
HDFN_J123647.29+621230.7	22.75	21.24	0.421	0.67	0.73	0.99	0.78	0.62	0.43	0.19	Spiral	4	
HDFS_J223254.09-603142.8	22.75	···	(0.494)	1.16	1.09	···	···	0.28	0.34	0.05	Spiral	2	
HDFN_J123652.72+621355.2	22.76	20.17	(1.578)	0.45	0.57	1.16	0.87	0.58	0.20	0.41	Pec	8	
HDFS_J223302.81-603325.2	22.79	···	(1.578)	0.89	0.86	···	···	0.23	0.22	0.23	Pec	4	
HDFS_J223257.06-603323.0	22.79	···	(0.583)	0.66	0.86	···	···	0.60	0.63	0.14	Early	0	
HDFN_J123653.45+621234.3	22.81	20.83	0.560	0.93	0.99	1.27	1.15	0.64	0.41	0.23	Spiral	4	
HDFN_J123657.73+621315.2	22.82	20.84	0.952	1.29	1.05	1.05	1.03	0.38	0.27	0.25	Pec	8	
HDFS_J223257.22-603305.5	22.83	···	(0.813)	1.37	1.05	···	···	0.10	0.20	0.13	Pec	7	
HDFS_J223253.24-603413.4	22.83	···	(2.388)	0.55	0.68	···	···	0.14	0.66	0.22	Early	1	
HDFS_J223252.16-603323.9	22.83	···	(1.578)	0.89	0.88	···	···	0.17	0.41	0.16	Spiral	4	
HDFS_J223255.24-603407.5	22.84	···	(0.402)	0.76	0.73	···	···	0.17	0.31	0.13	Spiral	5	S
HDFN_J123652.01+621209.7	22.85	21.00	0.457	0.67	0.79	0.98	0.91	0.38	0.43	0.14	Spiral	3	
HDFS_J223252.88-603317.1	22.86	···	(2.109)	1.42	1.29	···	···	0.05	0.24	0.29	Pec	6	
HDFS_J223249.40-603226.3	22.91	···	(2.704)	0.35	0.49	···	···	0.23	0.64	0.11	Early	2	
HDFN_J123641.42+621142.5	22.91	19.15	(2.489)	0.63	1.30	1.36	1.44	0.77	0.14	0.40	Pec	8	
HDFS_J223248.88-603216.1	22.93	···	(0.537)	0.92	1.07	···	···	0.61	0.37	0.14	Spiral	5	
HDFN_J123649.25+621148.5	22.93	20.25	0.961	1.50	1.64	1.41	1.24	0.27	0.46	0.08	Spiral	1	
HDFS_J223255.87-603317.8	22.94	···	(0.537)	0.85	0.90	···	···	0.20	0.37	0.18	Spiral	4	
HDFN_J123655.51+621402.7	22.95	20.86	0.564	1.22	1.18	1.30	1.11	0.75	0.27	0.14	Pec	4	
HDFS_J223249.50-603311.2	22.97	···	(0.515)	1.08	0.87	···	···	0.31	0.36	0.09	Spiral	3	
HDFS_J223249.34-603149.0	22.97	···	(0.370)	1.21	1.32	···	···	0.08	0.65	0.10	Early	0	
HDFN_J123656.92+621301.6	22.98	19.65	(0.959)	1.15	1.41	1.53	1.32	0.08	0.51	0.10	Spiral	1	
HDFN_J123648.59+621328.3	23.00	20.90	0.958	1.37	1.23	1.14	0.98	0.70	0.28	0.21	Pec	8	S
HDFS_J223249.85-603406.2	23.00	···	(1.393)	1.05	0.95	···	···	0.51	0.23	0.26	Pec	4	
HDFN_J123655.62+621249.4	23.01	21.61	(0.959)	1.29	1.05	1.08	0.78	0.15	0.25	0.21	Pec	8	
HDFN_J123651.98+621400.8	23.02	21.13	0.559	1.02	1.00	1.20	1.16	0.66	0.38	0.16	Spiral	4	
HDFN_J123644.83+621200.2	23.02	21.28	0.457	0.94	0.89	1.12	0.95	0.06	0.34	0.09	Spiral	4	

Table 1—Continued

ID[a]	I_{814}[b]	H_{160}[c]	z[d]	$V-I$[e]	$V-I$[f]	$J-H$[g]	$J-H$[h]	ϵ[i]	C[j]	A[k]	Auto[l]	RSE[m]	
HDFS_J223257.72-603408.7	23.03	···	(1.393)	2.46	2.58	···	···	0.04	0.66	0.19	Early	0	
HDFS_J223258.77-603323.5	23.03	···	(1.578)	-0.06	0.07	···	···	0.05	0.68	0.28	Early	-1	
HDFN_J123643.41+621151.6	23.04	21.01	(0.920)	0.63	0.68	0.93	0.95	0.22	0.59	0.14	Early	1	
HDFN_J123644.45+621141.5	23.05	20.95	1.020	1.11	0.99	1.17	0.74	0.76	0.18	0.28	Pec	8	S
HDFS_J223257.90-603349.1	23.08	···	(0.419)	0.82	0.85	···	···	0.37	0.29	0.10	Spiral	5	
HDFN_J123645.33+621154.5	23.11	20.13	0.372	1.93	2.02	1.45	1.39	0.15	0.54	0.08	Early	1	
HDFN_J123650.36+621418.7	23.11	21.40	0.819	1.06	1.08	1.04	0.96	0.52	0.26	0.11	Pec	8	
HDFN_J123651.98+621332.2	23.11	20.79	0.390	1.52	1.31	1.26	1.14	0.10	0.35	0.06	Spiral	4	
HDFS_J223258.11-603337.4	23.11	···	(2.291)	0.64	0.77	···	···	0.04	0.68	0.22	Early	-1	
HDFS_J223255.54-603217.6	23.15	···	(0.494)	0.82	0.77	···	···	0.45	0.37	0.14	Spiral	3	
HDFN_J123640.84+621203.0	23.15	20.39	1.010	1.24	0.90	1.13	1.10	0.54	0.29	0.34	Pec	8	
HDFS_J223248.36-603319.0	23.16	···	(0.455)	0.93	1.01	···	···	0.11	0.65	0.18	Early	-1	
HDFN_J123639.77+621228.9	23.16	21.24	(1.941)	0.46	0.68	0.92	0.87	0.59	0.29	0.25	Pec	8	
HDFN_J123650.84+621251.5	23.17	21.56	0.400	1.07	0.80	0.97	0.96	0.24	0.18	0.08	Pec	4	
HDFS_J223247.67-603252.4	23.18	···	(0.474)	0.95	0.82	···	···	0.51	0.28	0.12	Pec	4	S
HDFN_J123652.68+621219.8	23.19	21.45	0.401	0.67	0.77	1.04	0.94	0.36	0.52	0.12	Spiral	1	
HDFS_J223300.15-603319.0	23.20	···	0.540	0.99	0.98	···	···	0.11	0.43	0.06	Spiral	2	
HDFN_J123640.96+621205.4	23.21	21.18	0.882	0.54	0.63	1.26	1.13	0.23	0.43	0.28	Spiral	1	
HDFS_J223305.52-603321.3	23.21	···	(2.198)	0.97	1.08	···	···	0.31	0.62	0.30	Early	-1	
HDFN_J123646.87+621144.8	23.22	21.32	1.059	1.34	0.99	1.26	0.89	0.39	0.17	0.25	Pec	8	
HDFN_J123648.48+621316.6	23.23	21.36	(0.355)	1.02	1.16	1.21	1.12	0.15	0.45	0.06	Spiral	1	
HDFN_J123649.45+621316.6	23.23	19.34	(1.452)	0.79	1.04	1.34	1.35	0.62	0.43	0.26	Spiral	4	
HDFN_J123652.88+621404.8	23.24	21.30	0.498	1.15	1.11	1.08	0.94	0.29	0.30	0.39	Pec	8	
HDFS_J223249.18-603226.0	23.24	···	(2.704)	0.33	0.46	···	···	0.28	0.36	0.29	Pec	6	
HDFS_J223247.94-603251.1	23.24	···	(0.689)	1.63	1.79	···	···	0.07	0.64	0.37	Early	0	
HDFS_J223303.21-603329.7	23.25	···	(2.594)	0.51	0.60	···	···	0.11	0.35	0.48	Pec	6	
HDFS_J223250.68-603328.5	23.25	···	(1.786)	0.70	0.61	···	···	0.35	0.12	0.26	Pec	6	
HDFS_J223252.02-603214.9	23.25	···	(1.393)	1.41	1.19	···	···	0.40	0.31	0.05	Spiral	5	

Table 1—Continued

ID[a]	I_{814}[b]	H_{160}[c]	z[d]	$V-I$[e]	$V-I$[f]	$J-H$[g]	$J-H$[h]	ϵ[i]	C[j]	A[k]	Auto[l]	RSE[m]	
HDFN_J123656.42+621209.3	23.26	21.64	0.321	0.66	0.69	0.99	0.86	0.56	0.36	0.15	Spiral	4	
HDFS_J223248.56-603314.0	23.27	···	(0.634)	0.76	0.91	···	···	0.39	0.54	0.09	Early	1	
HDFS_J223253.70-603206.2	23.27	···	(1.941)	1.77	1.56	···	···	0.13	0.37	0.12	Spiral	8	
HDFS_J223248.24-603355.1	23.28	···	(0.661)	1.31	1.21	···	···	0.60	0.27	0.08	Spiral	6	
HDFN_J123644.20+621240.4	23.28	21.62	0.873	1.21	1.03	1.05	0.91	0.19	0.24	0.18	Pec	8	
HDFS_J223255.36-603355.0	23.30	···	(1.337)	2.37	2.45	···	···	0.06	0.61	0.17	Early	0	
HDFS_J223250.23-603145.8	23.31	···	(1.230)	1.38	0.98	···	···	0.19	0.20	0.19	Pec	6	S
HDFN_J123651.40+621420.9	23.31	21.81	(0.419)	0.71	0.66	1.00	0.88	0.49	0.29	0.13	Pec	4	
HDFS_J223250.72-603326.0	23.32	···	(1.578)	0.76	0.93	···	···	0.28	0.30	0.08	Spiral	7	
HDFN_J123647.79+621233.0	23.32	21.09	0.959	1.35	1.23	1.19	1.01	0.24	0.43	0.08	Spiral	1	
HDFS_J223300.49-603417.7	23.32	···	(1.132)	1.89	1.95	···	···	0.30	0.46	0.08	Spiral	1	
HDFN_J123648.32+621416.6	23.33	21.16	2.845	0.35	0.61	1.28	1.28	0.24	0.52	0.31	Spiral	4	
HDFN_J123656.13+621329.7	23.35	21.15	(1.180)	1.15	0.88	1.25	1.10	0.19	0.24	0.16	Pec	4	
HDFN_J123658.64+621221.8	23.36	21.66	0.682	0.88	0.97	0.98	0.93	0.30	0.45	0.18	Spiral	1	
HDFS_J223253.06-603217.1	23.36	···	(1.452)	1.31	1.06	···	···	0.62	0.24	0.12	Pec	5	
HDFN_J123649.82+621415.0	23.37	20.75	(1.786)	0.35	0.69	1.20	1.21	0.55	0.23	0.28	Pec	8	
HDFS_J223250.81-603141.6	23.38	···	(0.437)	0.90	0.92	···	···	0.19	0.26	0.05	Spiral	4	
HDFS_J223255.22-603410.2	23.41	···	(1.393)	1.16	1.18	···	···	0.01	0.23	0.07	Spiral	7	
HDFN_J123653.66+621417.6	23.41	21.74	0.517	0.96	0.90	1.10	0.99	0.68	0.35	0.11	Spiral	4	
HDFN_J123649.35+621155.1	23.42	21.90	(0.883)	0.54	0.77	0.78	0.72	0.15	0.60	0.13	Early	1	
HDFS_J223301.55-603410.8	23.44	···	(0.883)	1.32	1.23	···	···	0.65	0.36	0.15	Spiral	7	
HDFN_J123641.49+621215.0	23.44	20.23	(0.689)	1.92	1.90	1.35	1.37	0.17	0.63	0.09	Early	1	
HDFN_J123652.56+621201.7	23.45	21.78	(0.474)	0.86	0.93	0.95	0.89	0.28	0.69	0.25	Early	8	
HDFS_J223255.75-603333.8	23.46	···	(0.560)	1.23	0.80	···	···	0.12	0.16	0.12	Pec	6	S
HDFN_J123656.93+621258.2	23.46	19.33	0.529	1.01	0.98	1.12	1.04	0.49	0.39	0.10	Spiral	4	
HDFS_J223300.88-603325.9	23.47	···	(1.282)	1.07	0.91	···	···	0.62	0.19	0.22	Pec	6	
HDFS_J223251.11-603408.2	23.49	···	(0.355)	1.10	0.86	···	···	0.12	0.24	0.14	Pec	4	
HDFS_J223247.05-603316.0	23.51	···	(0.494)	1.39	1.46	···	···	0.12	0.62	0.24	Early	0	

Table 1—Continued

ID[a]	I_{814}[b]	H_{160}[c]	z[d]	$V-I$[e]	$V-I$[f]	$J-H$[g]	$J-H$[h]	ϵ[i]	C[j]	A[k]	Auto[l]	RSE[m]	
HDFN_J123647.18+621414.2	23.53	20.98	0.609	1.32	1.37	1.52	1.41	0.44	0.40	0.15	Spiral	4	
HDFS_J223253.09-603239.0	23.55	···	(0.537)	1.00	1.05	···	···	0.51	0.33	0.04	Spiral	2	
HDFN_J123655.16+621303.6	23.56	20.59	(4.266)	1.92	1.94	1.28	1.30	0.13	0.63	0.23	Early	1	
HDFN_J123648.99+621245.9	23.57	22.17	(0.437)	0.72	0.77	1.04	0.96	0.46	0.31	0.19	Pec	4	
HDFN_J123647.46+621330.1	23.58	21.90	(0.959)	1.35	1.31	1.08	0.90	0.17	0.23	0.09	Pec	4	S
HDFN_J123655.14+621311.4	23.60	22.14	(0.216)	0.50	0.58	0.94	0.89	0.29	0.38	0.13	Spiral	8	
HDFS_J223252.25-603152.8	23.60	···	(1.714)	0.80	0.90	···	···	0.31	0.45	0.08	Spiral	3	
HDFS_J223250.00-603345.2	23.64	···	(1.132)	1.02	0.77	···	···	0.32	0.21	0.14	Pec	3	
HDFS_J223254.98-603328.9	23.65	···	(1.042)	1.67	1.77	···	···	0.46	0.44	0.14	Spiral	2	
HDFN_J123651.95+621155.5	23.67	22.19	(0.155)	0.88	0.83	0.86	0.87	0.20	0.27	0.13	Pec	6	S
HDFS_J223255.83-603330.2	23.67	···	(0.207)	0.70	0.66	···	···	0.59	0.23	0.07	Spiral	3	
HDFN_J123647.18+621341.9	23.67	21.27	(1.452)	0.47	0.80	1.28	1.22	0.42	0.54	0.21	Spiral	1	
HDFN_J123646.52+621407.6	23.68	22.39	0.129	0.36	0.56	0.91	0.82	0.36	0.44	0.13	Spiral	1	
HDFS_J223249.09-603205.9	23.68	···	(2.291)	0.42	0.53	···	···	0.65	0.35	0.26	Pec	8	
HDFS_J223246.01-603407.3	23.71	···	(0.634)	0.61	0.81	···	···	0.33	0.41	0.33	Pec	2	
HDFN_J123645.96+621201.4	23.73	21.96	0.679	0.98	1.08	0.98	0.95	0.57	0.33	0.31	Pec	4	
HDFS_J223253.42-603333.4	23.74	···	(1.337)	1.19	1.20	···	···	0.54	0.28	0.21	Pec	5	S
HDFN_J123644.65+621227.4	23.74	21.27	2.268	0.59	0.68	1.26	1.18	0.28	0.43	0.19	Spiral	4	
HDFS_J223304.27-603331.8	23.75	···	(0.265)	0.96	0.82	···	···	0.17	0.25	0.18	Pec	3	
HDFS_J223254.79-603229.1	23.75	···	(0.883)	1.17	0.94	···	···	0.25	0.22	0.13	Pec	6	
HDFS_J223253.09-603206.7	23.75	···	(0.288)	1.01	1.11	···	···	0.04	0.56	0.08	Early	1	
HDFN_J123655.06+621329.1	23.75	22.72	(0.537)	0.87	0.77	0.93	0.93	0.26	0.27	0.12	Pec	4	
HDFN_J123655.59+621359.9	23.75	22.34	0.559	1.03	0.85	1.02	0.73	0.72	0.25	0.16	Pec	4	
HDFN_J123700.08+621225.3	23.77	21.76	(2.388)	0.45	0.48	1.15	1.07	0.47	0.23	0.31	Pec	8	
HDFS_J223252.25-603319.5	23.78	···	(0.244)	0.41	0.44	···	···	0.17	0.21	0.26	Pec	6	S
HDFN_J123649.99+621350.8	23.79	21.36	(1.086)	0.41	0.27	0.95	0.97	0.29	0.18	0.27	Pec	8	
HDFN_J123642.05+621130.5	23.79	23.02	(0.191)	0.42	0.47	0.68	0.65	0.60	0.21	0.31	Pec	4	
HDFS_J223253.85-603213.1	23.81	···	(1.862)	0.40	0.46	···	···	0.41	0.29	0.20	Pec	4	

Table 1—Continued

ID[a]	I_{814}[b]	H_{160}[c]	z[d]	$V-I$[e]	$V-I$[f]	$J-H$[g]	$J-H$[h]	ϵ[i]	C[j]	A[k]	Auto[l]	RSE[m]	
HDFS_J223248.48-603228.6	23.81	···	(1.452)	0.90	1.00	···	···	0.29	0.16	0.31	Pec	6	
HDFS_J223304.44-603409.0	23.81	···	(0.583)	1.32	1.06	···	···	0.26	0.24	0.13	Pec	3	
HDFS_J223255.77-603213.5	23.82	···	(0.689)	0.93	0.93	···	···	0.44	0.20	0.24	Pec	5	S
HDFN_J123639.44+621211.8	23.82	20.92	(0.959)	1.72	1.71	1.40	1.31	0.17	0.52	0.16	Spiral	1	
HDFN_J123639.73+621214.1	23.82	20.96	(0.883)	1.68	1.60	1.78	1.35	0.76	0.31	0.15	Spiral	4	
HDFS_J223302.12-603335.0	23.83	···	(0.455)	0.86	0.86	···	···	0.67	0.24	0.14	Pec	6	
HDFN_J123655.00+621314.8	23.83	22.25	(0.494)	0.76	0.79	1.02	0.93	0.36	0.36	0.15	Spiral	4	
HDFN_J123648.36+621412.4	23.85	22.14	(0.959)	1.00	1.09	1.11	0.85	0.60	0.19	0.24	Pec	6	S
HDFN_J123701.65+621225.9	23.85	21.29	0.974	0.94	1.04	0.72	0.88	0.44	0.38	0.24	Spiral	7	
HDFN_J123644.43+621244.1	23.86	21.00	(1.862)	0.33	0.38	1.24	0.92	0.66	0.30	0.37	Pec	6	
HDFN_J123645.31+621142.9	23.88	22.64	(0.560)	0.75	0.83	0.90	0.62	0.68	0.36	0.31	Pec	8	
HDFN_J123642.29+621134.8	23.89	22.01	(0.718)	1.04	1.23	1.12	1.16	0.26	0.34	0.18	Spiral	4	
HDFS_J223256.38-603144.3	23.89	···	(3.467)	0.83	0.71	···	···	0.47	0.19	0.11	Pec	8	
HDFN_J123649.47+621248.8	23.89	21.76	(1.941)	1.12	1.24	1.12	1.10	0.04	0.40	0.04	Spiral	1	
HDFS_J223300.87-603357.2	23.90	···	(1.393)	1.06	0.89	···	···	0.13	0.23	0.08	Pec	3	
HDFS_J223245.58-603347.3	23.90	···	(1.393)	0.70	0.69	···	···	0.37	0.22	0.26	Pec	6	S
HDFN_J123656.59+621252.8	23.90	20.42	(0.883)	0.67	0.72	1.75	1.44	0.43	0.24	0.17	Pec	4	
HDFN_J123638.61+621233.9	23.91	22.43	(2.198)	0.66	0.62	0.96	0.94	0.63	0.36	0.13	Spiral	4	
HDFS_J223247.78-603256.1	23.91	···	(0.689)	1.21	0.87	···	···	0.38	0.17	0.14	Pec	6	S
HDFS_J223259.85-603405.5	23.91	···	(1.644)	1.07	1.08	···	···	0.51	0.33	0.22	Pec	6	
HDFN_J123653.43+621221.7	23.92	21.85	(1.644)	0.23	0.38	0.68	0.72	0.24	0.42	0.32	Pec	4	
HDFS_J223257.10-603328.9	23.92	···	(0.689)	2.18	1.95	···	···	0.20	0.42	0.06	Spiral	1	
HDFS_J223251.97-603142.7	23.93	···	(0.494)	0.93	0.93	···	···	0.33	0.19	0.08	Pec	6	
HDFN_J123647.55+621252.7	23.94	22.24	0.681	1.09	0.98	1.11	1.05	0.62	0.29	0.10	Spiral	4	
HDFN_J123645.30+621152.3	23.95	21.22	2.803	0.44	0.59	1.52	1.39	0.73	0.14	0.36	Pec	6	
HDFS_J223251.65-603212.6	23.95	···	(1.282)	0.79	0.87	···	···	0.14	0.34	0.10	Spiral	2	
HDFS_J223255.87-603351.4	23.95	···	(0.515)	1.41	1.53	···	···	0.10	0.53	0.11	Spiral	1	
HDFN_J123649.04+621309.8	23.97	22.29	(1.132)	0.88	0.98	1.11	0.93	0.44	0.37	0.33	Pec	1	

Table 1—Continued

ID[a]	I_{814}[b]	H_{160}[c]	z[d]	$V-I$[e]	$V-I$[f]	$J-H$[g]	$J-H$[h]	ϵ[i]	C[j]	A[k]	Auto[l]	RSE[m]	R
HDFN_J123641.24+621202.9	23.98	22.30	3.210	0.41	0.56	1.27	1.21	0.39	0.31	0.44	Pec	6	
HDFN_J123648.27+621313.9	23.98	20.78	(0.959)	1.67	1.49	1.67	1.47	0.28	0.31	0.08	Spiral	8	
HDFS_J223252.70-603153.2	23.99	···	(1.180)	1.06	1.04	···	···	0.64	0.27	0.09	Spiral	3	
HDFS_J223254.03-603158.1	23.99	···	(1.452)	0.83	0.68	···	···	0.05	0.17	0.10	Pec	5	

[a]IAU designation from STScI SExtractor-based catalogs

[b]SExtractor mag_{best} from STScI catalogs

[c]H-band total magnitude

[d]Redshift (photometric redshift in parentheses). Spectroscopically confirmed stars are denoted by $z = -1.000$

[e]$V-I$ Color for central 5% of galaxy (see text for details)

[f]$V-I$ Color of total galaxy based on elliptical apertures defined from I-band image moments

[g]$J-H$ Color for central 5% of galaxy (see text for details)

[h]$J-H$ Color of total galaxy.

[i]1.0 - axial ratio of galaxy

[j]Central concentration

[k]Asymmetry

[l]Automated classification

[m]Ellis numerical classification

[n]Abraham visual classification

[o]Flag indicating the presence of a well-defined bulge (based on visual inspection)

[p]Flag indicating degree of object blending (based on visual inspection)

[q]Flag indicating clear galaxy peculiarity aside from blending/superposition

Table 2. Non-peculiar, unblended subsets from $I_{814} < 24$ mag sample

	Photometric Z			Spe	
Description of subset	N	$\langle\delta(V_{606}-I_{814})\rangle^{\dagger}$	$\sigma_{\delta(V_{606}-I_{814})}$	N	$\langle\delta(V_{606}$
Early type*					
Unblended, early-type galaxies	36	-0.083	0.448	11	-0.1
Unblended, early-type galaxies (RGA visual classification‡)	36	-0.083	0.488	12	-0.1
Unblended, early-type galaxies (RSE visual classification)	47	-0.220	0.490	19	-0.2
Unblended elliptical galaxies (RGA classed as E,E/S0)	26	-0.075	0.504	9	-0.1
Late type*					
Unblended late-type galaxies with obvious bulges	48	-0.526	0.330	24	-0.4
Unblended late-type galaxies with obvious bulges (RGA visual classification‡)	65	-0.544	0.309	29	-0.4
Unblended late-type galaxies with obvious bulges (RSE visual classification)	47	-0.538	0.288	19	-0.4
Unblended late-type galaxies with obvious bulges and area > 2000 pix	36	-0.480	0.226	19	-0.4
Unblended late-type galaxies with obvious bulges and (b/a) > 0.5	53	-0.540	0.309	22	-0.4

†Median central $\delta(V_{606} - I_{814})$ as defined in the text.

*Based on automated classifications unless specified otherwise.

‡Plotted in Fig.4